UNIVERSITÀ DEGLI STUDI DI TORINO

DIPARTIMENTO DI FISICA

SCUOLA DI SCIENZE DELLA NATURA

Corso di Laurea Magistrale in Fisica dei Sistemi Complessi

Tesi di Laurea Magistrale

Signatures of criticality in rat brain: beyond avalanches statistics

Laureanda:
Benedetta Mariani

Relatore:
Prof. Samir Suweis
Correlatore:
Prof. Stefano Vassanelli

Anno Accademico 2018/2019

ACKNOWLEDGMENTS

This work of thesis would not have been possible without the help and support of many people.
I thank my supervisors, Prof. Samir Suweis and Prof. Stefano Vassanelli, for being extremely helpful and open for discussions, and for believing in me. I thank my family and Riccardo, for always supporting me and caring for me. I thank my friends, the older ones from Padova, that have always been present even when far away, and the new, unexpected ones from Torino. Last but not certainly least, I thank my aunt Marinella, and her family; without her this surely wouldn't have been possible.

CONTENTS

CHAPTER 1

INTRODUCTION

A complementary strategy to the standard viewpoint in biology, which consists in analyzing each molecular component individually, is looking at complex biological problems from a global perspective, shifting the focus from specific details to integral aspects [1]. System approaches to biology rely on the fact that some phenomena of living systems, deriving from the interactions of many basic units, each one exhibiting some sort of nonlinear dynamics, are collective ones and might not be reducible to the understanding of elementary components as an individual basis ([2]). One of the most striking consequences of interactions among elementary constituents of matter (atoms, molecules, electrons, etc.) is the emergence of diverse phases, i. e. diverse types of macroscopic collective behavior. It is thus tempting to hypothesize that biological states might be manifestations of similar collective phases and that shifts between them could correspond to phase transitions. Some aspects of biological systems exhibit intermediate levels of organization, halfway between order and disorder. Remarkably it was conjectured that living systems could draw important functional advantages from operating right at the borderline between an ordered and a disordered phase, i.e. at the edge of a continuous phase transition or critical point [1]. For instance, being poised at the borderline between order and disorder could give a trade-off between robustness (resilience of the system state to external perturbations, which is a property of ordered phase) and flexibility (responsiveness to environmental stimuli, which is a feature of disordered phases) [5], [6].
In the last years scientists have begun to study also the human brain with this collective perspective. An adult brain consists of almost 10^{11} neurons and up to 10^{15} synaptic connections among them: the brain is indeed a system with an astronomical number of interacting elements, each one exhibiting plenty of non-linearities, and it is a fascinating challenge for a physicist to study its collective properties. Moreover, following the phase transitions approach to biological systems described above, in the last 30 years

some scientists moved the hypothesis that the brain could draw important functional advantages from operating at the edge of a continuous phase transition [2]. In 2003, the hypothesis found the first experimental support by J. M. Beggs and D. Plenz [3]. Yet, the critical brain hypothesis is not a consensus among the scientific community ([4]) and, even if there is richness of experimental evidence of criticality as regard spontaneous brain activity ([7], [8], [9], [10], [11], [12], [13]), little is known with respect to the impact of a sensory input on criticality.
This thesis aims at investigating the criticality hypothesis in the rat barrel cortex, which is the region of the primary somatosensory cortex that is identifiable in some species of rodents, that encodes tactile sensory inputs from the whiskers.
This work of thesis is organized as follows. In the next sections we introduce some concepts that are useful to understand and characterize interacting systems at criticality. The example of the continuous phase transition in the Ising model is presented, as well as the simplest toy model for spontaneous brain activity, the branching process, that displays non-equilibrium continuous phase transition between an absorbing phase and an active one.
In Chapter 2 a review of the critical brain hypothesis is presented: its conceptual implications on brain dynamics are explained, and it is described how to test criticality in experiments, reviewing the work done by J. Beggs and D. Plentz [3].
In Chapter 3 the main properties and synaptic circuits of the barrel cortex are described, giving a biological overview of the neural circuit under study. In Chapter 4 we present the data of Local Field Potentials (extracellularly recorded potentials with frequencies up to 500 Hz), which arise from trans-membrane currents passing through cellular membranes, and characterize the activity of the rat barrel cortex. The properties of the analyzed data are elucidated and it is explained how they have been obtained through the experimental setup.
In Chapter 5 the results are presented: in a first part, following the standard analysis triggered by J. M. Beggs and D. Plentz, statistics of neuronal avalanches are analyzed both at rest and after perturbations (controlled whisker deflection), on five different rats. In a second part, we go beyond the state of the art by showing an analysis based on statistical physics. In particular, signatures of criticality are searched analyzing both spatial and temporal correlations among signals recorded at different positions in the barrel. Additionally, a novel approach proposed by L. Meshulam et al. ([28]) is performed to detect the presence of non-Gaussian correlations in the system; this method unveils long range correlation using a Principal Component Analysis-based coarse-graining procedure, which is supposed to highlight if there is a gap in the eigenvalues spectrum of the covariance matrix of the dataset, hence suggesting an effective low dimensionality of the system and a departure from what one could expect in the presence of characteristic correlation lengths.
Finally in Chapter 6 the conclusions are drawn.

1.1 CRITICALITY AND SCALE INVARIANCE

A concept strictly related to criticality is the one of scale invariance: systems poised at a critical point exhibit scale invariance in many of their properties. In nature, different scales are usually decoupled and the physics at each one can be separately studied. However, there are situations, known as scale invariant or scale free, where broadly diverse scales make contributions of equal importance. Power-law distributions such as $P(x) = Ax^{-\alpha}$, where α is a positive real number and A is a normalization constant, are the statistical trademark of scale invariance or scaling. In fact, they are the only probability distribution functions for which a change of scale from x to Λx, for some constant Λ, leaves the functional form of $P(x)$ unaltered, i.e., $P(\Lambda x) = A(\Lambda x)^{-\alpha} = A\Lambda^{-\alpha}x^{-\alpha} = \Lambda^{-\alpha}P(x)$, in such a way that the ratio $P(\Lambda x)/P(x)$ does not depend on the variable x, i.e., it is scale invariant. As opposed to exponential distributions, power laws lack a relevant characteristic scale, besides finite size induced cutoffs.

1.2 CONTINUOUS PHASE TRANSITIONS

We now present the example of a continuous phase transition [15], in one of the most known equilibrium interacting particle model, the Ising model. If we consider a 2 dimensional lattice, then in each node i there is a spin that can take value $S_i = \pm 1$, spins interact and the system configuration is given by the Hamiltonian:

$$H = -J \sum_{\langle ij \rangle} S_i S_j \qquad S_i = \pm 1 \forall i \tag{1.1}$$

where the sum runs over the lattice's nearest neighbors. It is well known that in dimension $d > 1$ the Ising model displays a second order phase transition at a non-zero temperature $T = T_c$ [14]. In order to describe such transition we introduce a local order parameter, a physical quantity that vanishes in one phase and is non vanishing in the other. In the case of the Ising model, we consider the magnetization:

$$m = \frac{1}{N} \left\langle \sum_{i=1}^{N} S_i \right\rangle$$

which is in fact zero if the spins are randomly oriented, as it happens at high T. The interactions described by the Hamiltonian H are clearly short range interactions, and indeed at high temperature $T \gg T_c$ the model displays disorder, i.e. the magnetization is vanishing and the spins are randomly oriented. On the other side of the phase transition, for $T \ll T_c$ correlations are still short range, but here the magnetization is different from zero because the spins tend to be aligned. As we approach T_c the correlations length between the spins become more and more larger, leading to the formation of islands of alligned spins. Exactly at criticality, these islands exist at all scales. In addition, the largest fluctuations in the magnetization are observed at T_c: at this point a single spin perturbation has a small but finite chance to start an avalanche that reshapes the entire system state. Since no relevant scale can be defined, the physical

properties of the model turn out to be scale-free as well and therefore it makes sense to describe them via power laws. For instance, the order parameter scales as

$$m \sim |t|^{\beta}$$

where $t = \frac{(T-T_c)}{T_c}$ and β is called a critical exponent. A number of other exponents can be introduced. For instance, the zero field susceptibility is divergent as

$$\chi = \left.\frac{\partial m}{\partial h}\right|_{h=0} \sim |t|^{-\gamma} \tag{1.2}$$

where h is an external field with a corresponding Hamiltonian $H_h = -h\sum_i Si$ to be added to eq.1.1. We briefly remind that singularities like (1.2) only appear in the thermodynamic limit $N \to \infty$. Moreover, focusing on the correlation function

$$G(r) = \langle S_r S_0 \rangle - \langle S_r \rangle \langle S_0 \rangle$$

we expect that away from criticality, due to the short range nature of the microscopic interaction, it decays exponentially

$$G(r) \sim e^{-\frac{r}{\xi}}$$

where ξ is called correlation length and defines the typical scale of the system. However, close to the critical point the correlation length diverges as

$$\xi \sim |t|^{-\nu}$$

and exactly at the critical point the decay of the correlations becomes algebraic:

$$G(r) \sim r^{-(d-2+\eta)}$$

That implies that $\xi \to \infty$ as we approach the critical point (in the thermodynamic limit), so all scales are equally relevant. It is then evident how scale invariance and long-range correlations are characteristic properties of being in a critical point. We have thus learned from statistical physics that criticality can emerge as a collective behaviour in a many-body system with simple (e.g. short pairwise) interactions and its characteristics depend only on few details like dimensionality of the system and its symmetries.

1.3 NEURONAL AVALANCHES AND BRANCHING PROCESS

The cerebral cortex of mammalians is never silent, not even under resting conditions nor in the absence of stimuli; instead, it exhibits a state of ceaseless spontaneous electrochemical activity with very high variability and sensitivity. Neurons integrate presynaptic excitatory and inhibitory inputs from other neurons and fire an action potential when a given threshold is overcome, stimulating further activity. This basic process is similar to that seen in many other complex systems in which events like earthquakes, forest fires, and nuclear chain reactions emerge as one unit exceeds a

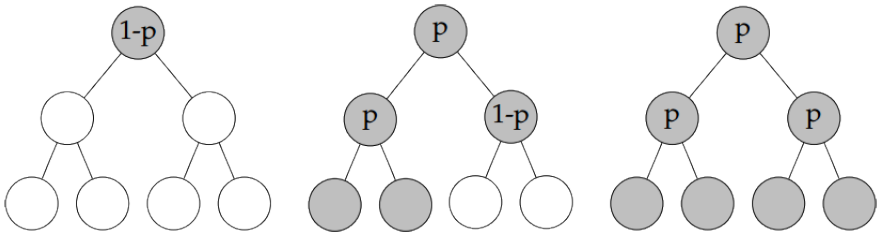

FIGURE 1.1: Some of the possible configurations of a branching process with $n = 2$, with avalanches of size $S = 1, 5, 7$ and boundary active sites $\sigma_2 = 0, 2, 4$.

threshold and causes other units to do so in turn, thereby initiating a cascade that propagates through the larger system. Neuronal activity can similarly be considered as a kind of neuronal avalanche in which activity propagates as individual neurons trigger action potential firing in subsequent neurons.

The branching process is maybe the simplest toy-model for spontaneous brain activity and scale-free avalanches, that exhibits a phase transition between an active phase and an absorbing one. Note that now we are properly referring to dynamical criticality, in the sense that this is a non-equilibrium phase transition in the underlying dynamical process and not simply in the statistics of equilibrium states. An avalanche starts with a single active site, which either relaxes with probability p, leading to two new active sites or it does not relax with probability $1 - p$ and leads to two inactive sites ([25]). This is called the first generation of the process. We define the size of an avalanche S as the number of active sites when the process dies or reaches the boundary. If the avalanche does not stop, we repeat the procedure for the new active sites until no active site remains. We can introduce boundary conditions in the problem in a natural way, by allowing for no more than n generations for each avalanche (see Figure 1.1). For the branching process, in the thermodynamic limit $n \to \infty$ there is a critical value, $p_c = 1/2$, such that for $p > p_c$ the probability to have an infinite avalanche is non-zero, while for $p < p_c$ all avalanches are finite, that is the system displays a second order phase transition with the average size of an avalanche $\langle S \rangle$ as the order parameter. Thus, $p = p_c$ corresponds to the critical case, where avalanches are power law distributed. We introduce the probability $P_n(S, p)$ of having an avalanche of size S in a system of size n (the maximum number of generations in the system) and the corresponding generating function. Then we have (see Fig. 1.1 for reference):

$$f_n(x, p) = \sum_S P_n(S, p) x^S$$

$$f_0(x, p) = x, \qquad f_1(x, p) = x(1 - p) + x^3 p$$
$$f_2(x, p) = x(1 - p) + x^3 p(1 - p)^2 + x^5 2p^2(1 - p) + x^7 p^3$$

and in general the following recursion relation

$$f_{n+1}(x, p) = x[(1 - p) + p f_n^2(x, p)]$$

holds. In the large n limit we expect $f_{n+1}(x,p) = f_n(x,p) = f(x,p)$ so that we can solve it to find:

$$f(x,p) = \frac{1-\sqrt{1-4x^2p(1-p)}}{2xp}$$

In order to determine the corresponding probability $P(S,p)$ we need to expand the generating function $f(x,p)$ as a power series in x. Recalling that the binomial theorem implies

$$\sqrt{1+x} = \sum_{k=0}^{\infty} \binom{\frac{1}{2}}{k} x^k = 1 - \sum_{k=0}^{\infty} \frac{2}{k+1} \binom{2k}{k} (-\frac{x}{4})^{k+1}$$

where we used the identity:

$$\binom{\frac{1}{2}}{k} = \frac{(-1)^{k-1}}{2^k k!} \binom{2k-2}{k-1}$$

Hence

$$f(x,p) = \sum_{k=0}^{\infty} \frac{1}{k+1} \binom{2k}{k} p^k (1-p)^{k+1} x^{2k+1}$$

Identifying $S = 2k+1$ we can write

$$P(S,p) = \frac{2}{S+1} \binom{S-1}{\frac{(S-1)}{2}} p^{\frac{S-1}{2}} (1-p)^{\frac{S+1}{2}} = \frac{2}{S+1} \binom{S-1}{\frac{(S-1)}{2}} \sqrt{\frac{1-p}{p}} [p(1-p)]^{\frac{S}{2}}$$

and now we shall consider the large S limit $1 \ll S \lesssim n$, i.e., we consider avalanches big enough bur still neglet the finite size of the system. In such case the Stirling approximation gives:

$$\binom{(S-1)}{\frac{(S-1)}{2}} \approx \frac{\sqrt{2\pi(S-1)}}{\pi(S-1)} \frac{[\frac{(S-1)}{e}]^{S-1}}{[\frac{(S-1)}{2e}]^{S-1}} = \frac{2^{S-1}}{\sqrt{\frac{\pi(S-1)}{2}}}$$

so that in this limit we find:

$$P(S,p) \approx \frac{1}{S} \sqrt{\frac{2(1-p)}{S\pi p}} [4p(1-p)]^{\frac{S}{2}} = S^{-\frac{3}{2}} \sqrt{\frac{2(1-p)}{\pi p}} \exp\left[-\frac{S}{S_c(p)}\right]$$

where the cutoff $S_c(p)$ is given by $S_c(p) = -\frac{2}{\log[4p(1-p)]}$. Notice that $S_c(p) \to \infty$ as $p \to p_c = \frac{1}{2}$, and this kind of divergence in indeed characteristic of a second order phase transition. At criticality we find the power law behavior

$$P(S) = P(S,p_c) = \sqrt{\frac{2}{\pi}} S^{-\tau}$$

with $\tau = \frac{3}{2}$.

The avalanche lifetime distribution $D(T)$ is defined as the probability to obtain an avalanche which spans T generations. After analogous calculations, one finds that

$D(T) \sim T^{-\alpha}$, with $\alpha = 2$, for $p = p_c$ [32].
To better understand the effect of finite size on avalanches, we introduce the random variable σ_n that describes the number of active sites in the n-th generation and its generating function

$$\phi_n(x,p) = \sum_k \mathbb{P}[\sigma_n = k]x^k$$

and in particular

$$\phi_1(x,p) = (1-p) + x^2 p.$$

Due to the iterative nature of the process we also have

$$\phi_{n+1}(x,p) = \sum_k \mathbb{P}[\sigma_n = k]\phi_1(x,p)^k = \phi_n[\phi_1(x,p)]$$

thus the expectation value is

$$\langle \sigma_{n+1} \rangle = \frac{\partial \phi_{n+1}(x,p)}{\partial x}\Big|_{x=1} = \phi_n'(1,p)\phi_1'(1,p),$$

since $\phi(1,p) = 1$. Therefore we have

$$\langle \sigma_1 \rangle = 2p$$

$$\langle \sigma_2 \rangle = (2p)^2$$

$$\vdots$$

$$\langle \sigma_n \rangle = (2p)^n$$

We expect the number of active sites at the boundary of the tree to be $\langle \sigma_n \rangle < 1$ in the subcritical case and $\langle \sigma_n \rangle > 1$ in the supercritical case. The critical case is then $\langle \sigma_n \rangle = 1$ for $p_c = \frac{1}{2}$.
Moreover, we expect that near the critical point the correlation length ξ is the only characteristic length of the system, in term of which all other lengths must be measured (this is the scaling hypothesis). Indeed, studies with the Renormalization Group and numerical simulations ([20]) suggest that there is a scaling relation between the duration T of an avalanche and its linear extent ℓ: $T \sim \ell^z$. As well, they suggest that the fractal dimension of the avalanches is $\frac{1}{\sigma\nu}$, meaning that the spatial extent ℓ of an avalanche is proportional to $S^{\sigma\nu}$. Then, if we look at all avalanches of a certain duration T, they will have a distribution of sizes S around some average $\langle S \rangle (T)$. If the time scale is expanded by a small factor $B = 1/(1-\gamma)$, then the rescaling of the size will also be small, say $1 + \delta\gamma$.

$$\langle S \rangle (T) = (1 + \delta\gamma)\langle S \rangle ((1-\gamma)T)$$

Making γ very small yields the simple relation $\delta \langle S \rangle = T\frac{d\langle S \rangle}{dT}$, which can be solved to give the power law relation $\langle S \rangle (T) = S_0 T^{\delta}$. The exponent δ is another critical exponent. Comparing this relation between $\langle S \rangle (T)$ and T with the relative scaling of

S and T with respect to the linear extent of an avalanche ($S \sim \ell^{\frac{1}{\sigma\nu}}$, $T \sim \ell^{z}$) one easily obtains that $\delta = \frac{1}{(\sigma\nu z)}$. Then, noting that

$$\int P(S)dS = 1 = \int D(T)dT$$

with $P(S)$ the sizes distribution of the avalanches and $D(T)$ the lifetimes distribution of the avalanches, calling N_1 and N_2 two normalization constants, one gets:

$$\frac{\int S^{-\tau}dS}{N_1} = \frac{\int T^{-\alpha}dT}{N_2}$$

$$\frac{N_2}{N_1}S^{-\tau+1} \sim T^{-\alpha+1}$$

$$C\ell^{\frac{-\tau+1}{\sigma\nu}} \sim \ell^{(-\alpha+1)z}$$

Therefore $\ell^{\frac{1}{\sigma\nu z}} = \ell^{\delta} \sim \ell^{\frac{(\alpha-1)}{(\tau-1)}}$, obtaining the following exponents relation between $\frac{1}{\sigma\nu z}$ (from now on called δ), α and τ: $\delta = \frac{\alpha-1}{\tau-1}$.
This relation is universal and it is valid among different models, as far as they display avalanche size distribution $P(S) \sim S^{-\tau}$, avalanche lifetimes distribution $D(T) \sim T^{-\alpha}$ and the relationship $\langle S \rangle (T) \sim T^{\delta}$. For example, it is verified by J. Sethna in a model of the avalanches in presence of Barkhausen noise [20]. The values of these exponents define different universality classes.
The predicted value for δ in the critical branching process is 2, and, together with the exponents $\tau = \frac{3}{2}$ and $\alpha = 2$, belongs to the same universality class of other models such as the contact process, directed and isotropic percolation, susceptible-infected-susceptible, and a large list of prototypical models for spreading/propagation dynamics above their respective upper critical dimensions. This universality class is called mean-field directed percolation (MF-DP) [21].

CHAPTER 2

CRITICAL BRAIN HYPOTHESIS

Around 1950s, direct analogies between the brain and ferromagnets were employed in the theory of neural networks ([33], [34]). During the 80s, the field of attractor neural networks, dynamical networks that evolve towards stable patterns over time, had largely been studied by statistical physicists to model neuronal processes such as associative memory [37]. Theoretically the critical brain hypothesis had been primarily explored using computational models of neural networks by Herz and Hopfield in 1995 [35], which highlighted that self organized criticality (known as SOC [38]) theory could be used to model earthquakes and neuronal avalanches. However, only during the past decade experiments have begun to uncover direct support of the critical brain hypothesis. In particular the experimental work by John Beggs and Dietmar Plenz (2003) [3] has triggered an avalanche of research, with thousands of studies referring to it. The hypothesis that the brain operated at a critical point is attractive for two reasons, on a conceptual level and on an experimental level ([16]).

On a conceptual level, criticality has been shown to maximize a number of properties that are considered favourable for computation [1] . Indeed, large scale correlations would allow a coherent global response to external stimuli as well as an optimal information transmission, and at the same time the divergent susceptibility of the system would translate into a high sensitivity to sensory stimuli. In Ref. [16] they showed how three specific functional properties of cortical networks are optimized near criticality: dynamic range, which is the range of stimulus intensities that are distinguishable based on the population response of the network, the fidelity of information transmission, and information capacity, which characterizes the repertoire of activated neural assemblies available to a neural population and imposes limits on many information-processing tasks including, but not limited to, information transmission.

On an experimental level, there is considerable evidence in support of the criticality hypothesis. However assessing criticality experimentally is more intricate than first

thought, and critical brain hypothesis is still a matter of debate among scientists [17]. The original interpretation of the critical brain hypothesis, as formulated by J. Beggs and D. Plentz, is that brain circuits would gain advantages from being poised at the borderline between a phase where activity rapidly dies out and a phase where activity is amplified over time, so the transition would happen between an absorbing phase and an active one. An intuitive understanding of this interpretation of criticality is given by the concept of balance. Imagine a small piece of cortex including 100 neurons that are completely interconnected and p is the likelihood that one spike (one neuron activity) causes each other neuron to fire. If p is $\frac{1}{2}$ then one spike is likely to cause half of the neurons in the network to fire. Subsequently those 50 spikes are likely to cause all neurons to fire. In this case a single spike ignites a runaway chain reaction that never stops. Next, suppose that p is for example $\frac{1}{1000}$. In this case 10 spiking neurons are required to generate just 1 single subsequent spike (on average), which in turn will cause none (on average). Apparently, p equal to $\frac{1}{1000}$ entails activity that dies out almost immediately. The balanced p is $\frac{1}{100}$. In this case, one spike is likely to cause one subsequent spike; the activity leads to a reverberating response to the initial spike that does not overwhelm the entire network. More generally, in any network in which each neuron connects to N postsynaptic neurons, p must be $\frac{1}{N}$ to achieve balance. When balanced, the simple model described above is an example of a network operating at criticality. When imbalanced, such as when $p = \frac{1}{2}$ or $p = \frac{1}{1000}$, the network is not at criticality; rather, these two examples are referred to as *supercritical* and *subcritical* state, respectively. Therefore this type of criticality indicates a transition between an "active" and a "silent" state. Neverthless other types of criticality may exist.

For example, recent studies have stressed how the signatures of a critical state might be dependent on the level of synchronization in the firing activity of the neurons: in Ref. [24] they analyzed neuronal activity in deep layers of the primary sensory cortex of urethane-anesthetized rats and found that rather, the critical point separated a phase in which neurons fired synchronously and a phase characterized by largely incoherent firing of neurons. These findings have been also theoretically confirmed by a Landau-Ginzburg theory of cortex dynamics [36]. Moreover, experimentalists found stronger signs of criticality in synchronized neural waves, which occur most often during deep sleep, than in the more scattershot firing patterns of alert animal brains [39]. These results suggested that criticality might not be related to optimal brain information processing, as previously thought.

Moreover, little is known as regard the impact of sensory input on criticality. It has been proposed that nervous systems self-adapt to criticality, and some computational and theoretical models have shown that adaptation to sensory inputs and to the environment could maintain the critical network dynamics [18]. However, in Ref. [19] they argued that these previous works did not consider the impact of strongly driven regime that is expected during intense sensory input. Indeed, in their work they showed that strong sensory inputs may increase the overall excitability of the network and potentially elicit cortical networks dynamics that are not critical, and then adaptive changes in the network rapidly tune the system to criticality. This topic remains largely unstudied, and further research is needed to clarify the principle governing the adaptation to sensory inputs of neuronal networks.

2.1 NEURONAL AVALANCHES

In a remarkable breakthrough, J. Beggs and D. Plenz (2003) were the first to succeed at resolving the internal spatiotemporal organization of the outbursts of neuronal activity [3]. They analyzed mature cultures as well as acute slices of rat cortex and recorded spontaneous local field potentials (LFPs) (see section 4.1 for more details on LFPs), which provide coarse-grained measurements of electro-chemical activity, at different locations and times. Local events of activity are defined as peaks of the LFP signals. They temporally resolved these outbursts of activity grouping in spatio-temporal clusters consecutive LFP peaks with inter-peak intervals not exceeding a temporal threshold. These outbursts of activity then resulted in cascade of successive local events, organized as *neuronal avalanches*, interspersed by periods of quiescence. The avalanche sizes (i.e. number of local events each one includes) and lifetimes were found to be distributed as power laws with exponents $\tau \approx \frac{3}{2}$ and $\alpha \approx 2$, respectively. They noted that these exponents coincide with the ones of the critical branching process, and then supposed that this model might adequately describe propagation of activity in the cultured neural network. They indeed used the branching parameter σ to describe the activity propagation in the cortical cultures. By definition, σ is the average number of descendants from one ancestor and, intuitively, was defined as the average number of electrodes activated in the next time bin, given a single electrode being active in the current time bin:

$$\sigma = \sum_{d=0}^{n_{max}} d \times p(d)$$

where d is the number of electrode descendants, $p(d)$ is the probability of observing d descendants, and n_{max} is the maximal number of active electrodes. $\sigma > 1$ would represent a super-critical state in which an increasing number of electrodes would be activated at each step, eventually leading to an unstable runaway activation of the network. If $\sigma < 1$ (sub-critical state), activity would decrease over successive steps. If $\sigma = 1$ (critical state), activity at one electrode would lead to activity in one other electrode on average, keeping the network at the edge of stability. They found that σ calculated on their data was remarkably close to the critical value 1. So, they strongly supported a critical branching process as the mechanism behind the power law distributions in cortical networks.
Moreover, in their experiments the mean temporal profile of neuronal avalanches of widely varying durations was found to be quantitatively described by a single universal scaling function, and scaling relationships between the measured exponents were fulfilled:

$$\delta = \frac{\alpha - 1}{\tau - 1} \tag{2.1}$$

where δ is given by:

$$\langle S(T) \rangle \sim T^{-\delta} \tag{2.2}$$

Where S represents the size of an avalanche and T its duration ([20], [19]).

2.2 How to test the criticality hypothesis in experiments

In order to test the criticality hypothesis in experiment one requires a research strategy that achieves two criteria:

1. a means of altering the overall balance of interactions between the neurons;
2. a means of assessing how close to criticality the cortex is operating.

In computational models, the control parameter is tunable by the modeler and it is easy to determine what value of the parameter results in criticality. In experiments, there are some strategies to achieve the first criterion. For example, one may apply pharmacological antagonists of excitatory synapses, creating an imbalance favoring inhibition. However, the second criterion presents a challenge because it is not feasible to directly measure the overall balance of interactions in even a small piece of cortex [16]. Moreover, meeting the second criterion is especially crucial in experiments because one's attempt to alter the cortical balance may fail because of unexpected compensatory mechanisms that restore the balance without the experimenter's permission. One solution is to carefully assess network dynamics, testing for indirect signatures of criticality that are predicted by the theory of phase transitions.

1. As seen in the work of Beggs and Plentz, the main approach to detect criticality is to search for *neuronal avalanches* whose sizes and lifetimes follow power-law distributions. Importantly, the second criterion above can be achieved with an analysis strategy that assesses how close the system is to criticality based on how close the observed dynamics are to neuronal avalanches.
2. On another hand, as regard large scales, another signature of criticality is the presence of long-range correlations in space and time (theory of phase transitions predicts indeed the divergence of the correlation length in the termodinamical limit), and moreover, using an analogy with the Ising model, a near-zero magnetization, or, equivalently, the presence of anticorrelated cortical states [2].

Similar avalanches to the one observed by Beggs and Plentz have been observed in vitro ([7], [8]) and in vivo for different species ([9], [10], [11], [12], [13]) and across resolution scales, from single neuron spikes to rather coarse-grained measurements. All this evidence regarding neuronal avalanches seems to make a strong case in favor of criticality. However, some caveats need to be made. There is some ambiguity in the next aspects [1]:

1. Thresholding: A source of ambiguities in extracting (discrete) events from (continuous) time-series analyses comes from thresholding; i.e., signals at any given spatiotemporal location need to overcome some threshold to be declared an event of activity.
2. Time binning: Avalanches can be defined only by employing a criterion to establish when an avalanche starts and when it ends. This requires setting a discrete time binning to be applied to the data: an avalanche starts when a time bin with some activity within it follows a series of preceding consecutive quiescent ones and ends when a new quiescent time bin appears. This introduces some ambiguity, and the measured avalanche exponents have been shown to be sensitive to the choice of the time bin. However, taking the time bin to coincide with the mean inter-event interval, the critical branching process exponents

seem to be systematically recovered. Further work is needed to mathematically clarify this important issue.

3. Subsampling: A related problem is that of subsampling as a result of observational and resolution limitations. Owing to these factors the statistic is not complete, and this might affect the shape of the observed distributions.

As an additional fact, one could argue that the power-law is an uninformative distribution. Indeed, diverse generative processes for the emergence of power-laws exist, and not all power-law distributions can be taken as a signature of criticality. For example, it has been shown how random walk processes display power-laws as regards the distribution of return times to the origin and the areas covered by their excursions before returning to the origin ([1], [21]). This series of observations, taken together, seems to shed some doubts on evidence in favor of criticality relying on avalanches. However, a stringest test for criticality based on neuronal avalanches is to verify whether the exponents of the power-laws are compatible with the relations 2.1 and 2.2. Indeed, at criticality one expects that many properties are distributed as power-laws, whose exponents are not all independent but instead respect a relationship.

CHAPTER 3

THE BARREL CORTEX

3.1 NEURONS: THE UNITS OF THE CORTEX

Neurons are electrically excitable cells that communicate with other cells via specialized connections called synapses. A typical neuron consists of a cell body (*soma*), dendrites, and a single axon.

The dendrites are subtle and profusely branched filaments that depart from the soma and collect information from other input neurons. The soma integrates the information collected by the dendrites. The axon is a major filament. It leaves the soma at a swelling called the axon hillock. It branches but usually maintains a constant diameter. At the farthest tip of the axon's branches there are the axon terminals, where the neuron can transmit a signal across the synapse to another cell, through the release of neurotransimitters (chemical messengers that are received by receptors on target cells). Neurons, as excitable cells, have the ability to react to a sufficient strong stimulus with a variation in the permeability of the cell's membrane: that lets ions flux across the membrane and change the value of the potential across the membrane.

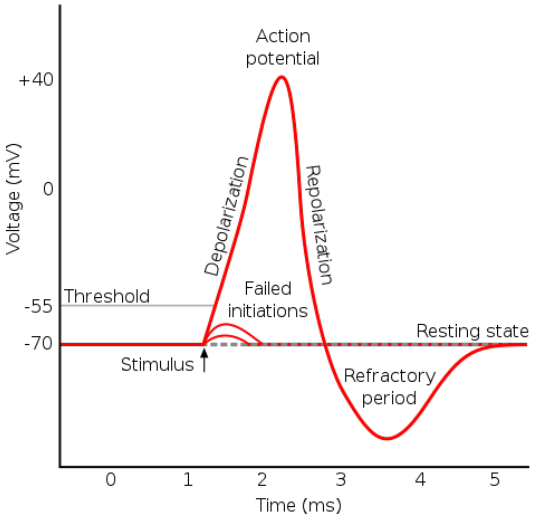

FIGURE 3.1: Action potential

Indeed, at rest, a typical neuron has a resting potential (potential across the membrane)

of -70mV. This means that the interior of the cell is negatively charged relatively to the outside. It is then called *polarized*. The ions which have an important role in the maintenance of this resting potential are Na^+, which is more present in concentration on the outside of the membrane than in the inside, and K^+, which is more present in the inside of the cell. If the net input a neuron receives is sufficient to drive the neuron's membrane potential above some threshold (usually between $-55mV$ and $-45mV$), then the neuron undergoes an action potential. (Fig. 3.1).
Indeed, the reaching of the threshold value results in the opening of the Na^+ voltage-dependent channels, so the Na^+ ions follow their concentration gradient, and the inside of the cell becomes positive (*depolarized*). After a delay, also the K^+ channels open, which will instead repolarize the neuron. The action potential will propagate through the axon, and this results in electrochemical signals being transmitted through the synapses: once the action potential reaches the axon terminals, a neurotransmitter is released in the inter-synaptic space, which will reach the membrane of the postsynaptic neuron and bind to specific receptors. In typical excitatory synapses, the neurotrasmitter determines the opening of ligand-dependent channels for Na^+ or Ca^{++} causing a depolarization of the neuron (post-synaptic excitatory potential): if the depolarization reaches the threshold, an action potential will be generated. There are also inhibitory sinapses: in this case the post-synaptic neuron will hyper-polarize instead.

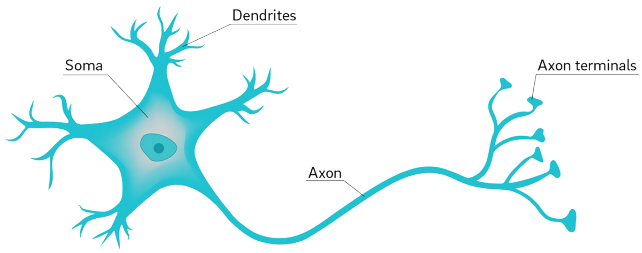

FIGURE 3.2: Schematic representation of a neuron

3.2 THE BARREL CORTEX

The barrel cortex is the region of the primary somatosensory cortex (S1) that is identifiable in some species of rodents, that receives input from the whiskers via the thalamus. Its high degree of cortical segmentation into vertical columns and horizontal layers advantages scientific investigation: researchers have intensively studied the barrel cortex as a model of neocortical column. The whisker-related barrel column is a cylindrical structure spanning vertically the six layers of barrel cortex although its border is defined exclusively by spatially aligned sub-cellular structures in layer 4. Each column measures about 300 μm in width and runs through the entire depth of the cortex, about $2mm$ long in rats. Each barrel-column is composed of an archetypical circuit that is repeated in each column, with each large barrel containing approximately 2000 neurons. Cortical neurons divide into two major classes. Principal cells are neurons that use the

excitatory neurotransmitter glutamate. They are usually pyramidal in shape: one of the main structural features of a pyramidal neuron is the conic shaped soma, after which the neuron is named. Other key structural features of a pyramidal cell are a single axon, a large apical dendrite, multiple basal dendrites, and the presence of dendritic spines. Principal cells respond selectively to specific features of sensory stimuli, and contact local and distant targets through extensive axonal projections. Principal cells comprise approximately 80% of cortical neurons in rodents, and fall into multiple classes distributed across and within cortical layers. The remaining approximately 20% are interneurons that release the inhibitory neurotransmitter GABA and make mostly local connections.
By using their whiskers, rodents can build spatial representations of their environment, locate objects, and perform fine-grain texture discrimination. This sensory system is therefore an attractive model for investigating active sensory processing and sensorimotor integration, as well as the ongoing basal activity spontaneously generated in these cortical circuits.

3.2.1 FROM WHISKER TO CORTEX

The most important synaptic pathways signaling whisker-related sensory information to the neocortex have begun to be characterized.
The structure that anchors a whisker to the skin is called follicle. Deflection of a whisker is thought to open ion channels in nerve endings of sensory neurons innervating the hair follicle.
Afferent signals coming from the follicular innervation travel past the cell bodies of the trigeminal ganglion (TG) [1] and continue along the central branch to form synapses in the trigeminal nuclei [2] (TN) of the brainstem. The trigeminal nuclei convey afferent vibrissal information to the thalamus [3] via three main parallel pathways ([26]). These pathways are called lemniscal, paralemniscal and extralemniscal. The lemniscal pathway starts from the neurons in the principal sensory trigeminal (PrV) nucleus, which are clustered into *barrelettes*. The axons of these neurons travel, via the lemniscal

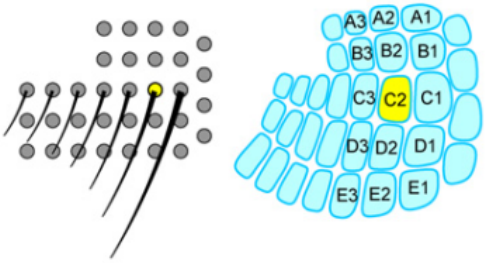

FIGURE 3.3: Whiskers and barrels

[1] The trigeminal ganglion is a sensory ganglion of the trigeminal nerve that lies in a cavity on the base of the skull, i.e. the fifth cranial nerve responsible for sensation in the face.
[2] A cranial nerve nucleus is a collection of neurons in the brain stem that is associated with one or more cranial nerves.
[3] The thalamus is a large collection of neuronal groups within the brains of vertebrates, situated between the cerebral cortex and the midbrain; it participates in sensory, motor, and limbic functions (regulation of consciousness, sleep and alertness).

pathway, to the *barreloids* of the ventral posterior medial nucleus (VPM) of the thalamus. Both barrelettes and barreloids are well-defined groups of neurons that represent single whiskers. Neurons in a given module respond principally to the corresponding whisker, thus defining a single-whisker receptive field for the trigeminal sensory neurons. The axons of VPM neurons within individual barreloids project to the primary somatosensory neocortex forming discrete clusters in layer IV, which form the basis of the barrel map. The clear anatomical maps segregating neighboring whisker representations strongly suggest a labeled line single-whisker signaling pathway from the periphery to the barrel cortex. There are obvious anatomical structures termed *barrels* in layer IV of the primary somatosensory neocortex, which are laid out in a near identical pattern to the whiskers, that are separated from each other by narrower zones called septa. The standard nomenclature for both whiskers and barrels consists of the rows A-E and the arcs 1, 2, 3, etc. The C2 whisker follicle and the C2 barrel are highlighted in yellow in figure 3.3.
The recently discovered extralemniscal pathway signals through a ventrolateral strip of the VPM to the secondary somatosensory cortex and the septal regions of S1. There is also an important paralemniscal pathway, projecting to the posterior medial (POM) nucleus of the thalamus, which in turn primarily innervates layer I and Va of the primary somatosensory cortex, the secondary somatosensory cortex and the motor cortex. Unlike the lemniscal pathway, the paralemniscal pathway is not spatially specific, integrating multiple-whisker information and defining a multi-whisker receptive field.
Direct mapping of the electrical activity of the cortex can be obtained by voltage-sensitive dye (VSD) imaging ([26]). The VSD diffuses into the superficial layers of the cortex and changes fluorescence rapidly and linearly with respect to membrane potential. It has been shown that measuring with VSD a single brief deflection of the C2 whisker evokes a sensory response with complex spatiotemporal dynamics. The earliest response occurring $\sim 10ms$ after whisker deflection is highly localized to its corresponding C2 barrel column. However, in the following milliseconds the response increases in amplitude and propagates horizontally to cover a large fraction of the barrel cortex. The overall impression with VSD imaging is therefore that although cortical columns are functionally present, they only last a few milliseconds and then large areas of the cortex become depolarized. The propagating VSD responses therefore indicate that large numbers of neurons across the cortical map are influenced by a single-whisker deflection.

3.2.2 SYNAPTIC CIRCUITS OF THE BARREL CORTEX

The synaptic circuits in the barrel cortex that are likely to underlie the sensory response to a simple stimulus in an anesthetized animal have begun to be examined in detail. Sensory information related to a single-whisker deflection arrives in the primary somatosensory neocortex mainly via the thalamocortical innervation of the neurons located in the VPM. The axon of a VPM neuron primarily innervates a single somatotopically aligned layer IV barrel. As a first-order approximation, a single deflection of the C2 whisker evokes a volley of near-synchronous thalamic input to arrive within layer IV of the C2 barrel column. Thalamic axons make synapses on a diversity of

dendrites in the layer IV barrel. The excitatory layer IV barrel neurons have dendritic and axonal arbors laterally confined to a single layer IV barrel, and the thalamic input arriving in a single layer IV barrel therefore largely remains confined to that barrel for the initial step of cortical processing. The excitatory layer IV axons prominently innervate layer II/III in the immediately overlying area, therefore structurally defining a cortical column delimited laterally by the width of the layer IV barrel. A stimulus delivered to a layer IV barrel first causes depolarization within the layer IV barrel, which then in the subsequent milliseconds spreads to depolarize neurons in layer II/III in a strictly columnar fashion. The axonal aborization of the layer II/III neurons extends well beyond the boundaries of a barrel column, and since single-whisker deflections can drive action potential firing in layer II/III neurons, the output of these neurons will depolarize neurons widely distributed across the barrel cortex, likely underlying the spreading VSD signal. In addition to contacting other layer II/III neurons, the axons of the layer II/III neurons also form a prominent input to layer V. Synaptic integration in layer V neurons is complex since they can also receive substantial direct thalamic input along with excitatory input both from layer IV and from other neurons in the infragranular layers (layers V and VI) (Fig. 3.4 C). In addition to the canonical excitatory synaptic circuit from VPM to layer IV barrel to layer II/III to layer V, there are a number of other important synaptic connections that are likely to play prominent roles during information processing in awake animals. Perhaps the most important are the long range corticocortical inputs from secondary somatosensory cortex and motor cortex and the likely influence of POM thalamic input during certain behaviors. POM input arrives predominantly in layer I and Va, defining the starting point of the paralemniscal cortical processing pathway. Layer Va in turn projects to layer II.
In figure 3.4 it is important to notice that barrel layer IV neurons are intrinsic elements of all three microcircuits ([27]).

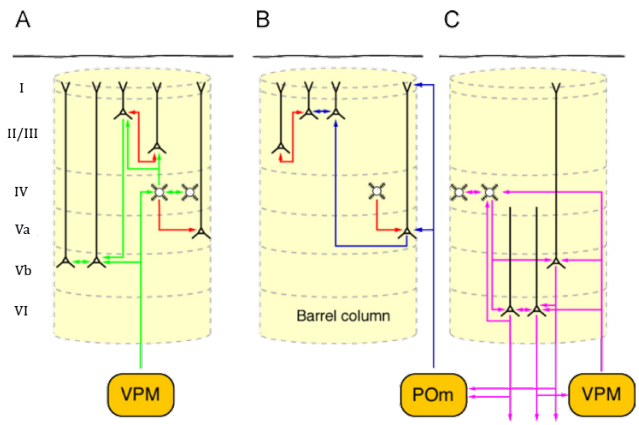

FIGURE 3.4: Simplified scheme of parallel neocortical microcircuits in the barrel cortex. (A) The canonical microcircuits receiving lemniscal thalamic input from the ventroposterior medial nucleus (VPM) predominantly in layer IV. (B) Microcircuits involved in the processing of signals arriving from the paralemniscal pathway (C) Synaptic connections involved in the thalamocorticothalamic feedback circuit between layer IV neurons, Vb and VI cells and the thalamic nuclei.

CHAPTER 4

EXPERIMENTS AND DATA

4.1 LOCAL FIELD POTENTIALS

Local field potentials (LFPs) are extracellularly recorded potentials with frequencies up to 500 Hz. The high frequency part of the recorded potentials provides instead information about the spiking activity (action potentials) of the neuron located around the electrode. Recently, the interest in LFPs has undergone a resurgence [23]. Key reasons are the growing capacity for streaming continuous data from multiple electrodes and the development of multicontact electrodes for high-density recordings across areas and laminae. This has enabled recordings of LFPs at tens to hundreds of sites simultaneously and has offered a unique window into key integrative synaptic processes in cortical populations: the LFP captures integrative synaptic processes that cannot be measured by observing the spiking activity of a few neurons alone. However, owing to its numerous potential neural sources, the LFP is more difficult to interpret than are spikes in terms of the underlying neural activity. By using computational methods of analysis and modelling, systematic investigations of the link between the recorded LFPs and various types of underlying neural activity can be pursued. The past decade has seen the refinement of a well-founded biophysical forward-modelling scheme that is based on volume conductor theory (the word "forward" denotes that the extracellular potentials are modelled from neural transmembrane currents; inverse modelling, by contrast, estimates neural currents from recorded potentials), in particular a forward-modelling scheme based on *multicompartmental neuron models* has been established. The multicompartmental models are neuron models in which dendrites and/or axons are divided into several compartments so that the membrane potential throughout each compartment can be assumed to be the same.

4.1.1 LFPs FROM SINGLE NEURONS

Extracellular potentials arise from transmembrane currents passing through cellular membranes in the vicinity of the electrode. For cortical LFPs, contributions from synaptic inputs appear to be the dominant component.

Forward-modelling studies have provided important insights into how LFPs from synaptic input currents (and their accompanying return currents) vary with a neuron's dendritic morphology and the positions of the synapse and recording electrode. This studies has shown for example how the LFP from an excitatory synaptic current onto an apical branch of a pyramidal neuron (Fig. 4.1) is negative close to the synapse but positive around the soma, where the accompanying return currents are strong (owing to the large surface area of dendrites in the soma region). A similar synapse onto the basal dendrites results in a dipole-like contribution of opposite polarity, with negative currents around the soma and positive currents at the apical dendrites (an apical dendrite is a dendrite that emerges from the apex of a pyramidal cell while a basal one emerges from the base of a pyramidal cell). Positive currents leaving the extracellular medium - for example, positive charges entering neurons - are conventionally termed current sinks, whereas positive currents entering the extracellular medium are termed current sources. The cortical pyramidal neurons have a characteristic open-field structure: a geometrical arrangement of synaptic inputs onto neurons in which, on average, there is a substantial spatial distance between synaptic currents and the bulk of the return currents. This implies a sizable current dipole, and it is thought that a superposition of many such open-field generators dominates cortical LFPs.

Another key qualitative feature of the LFP is that signals close to the apical synapse have narrower temporal traces (that is, they have higher temporal frequencies) than do signals close to the soma, which are dominated by return currents in the soma region.

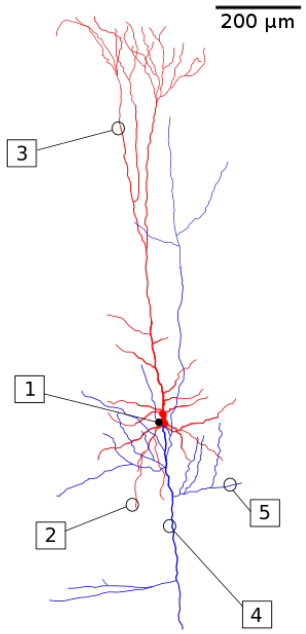

FIGURE 4.1: A reconstruction of a pyramidal cell. Soma and dendrites are labeled in red, axon arbor in blue. (1) Soma, (2) Basal dendrite, (3) Apical dendrite, (4) Axon, (5) Collateral axon.

4.1.2 HOW LOCAL IS THE CORTICAL LFP

Although synaptic input and the associated return currents may dominate cortical LFPs, spikes also contribute to the signal. However, the question of how local the signal is - that is, the spatial extent of the cortical region that generates a recorded LFP - is still vigorously discussed. A study in Ref. [22] investigated disc-like laminar populations of pyramidal neurons surrounding a recording electrode. When these neurons receive

synaptic inputs, their LFP contributions add up linearly to produce the net population LFP. Everything else being equal, a neuron close to the electrode contributes more to the population LFP than a neuron further away. However, geometrical reasoning implies that with a constant density of neurons in the disc-like population, the number of neurons at a particular distance from the electrode increases linearly with the distance. Hence, the relative contributions from the rings of neurons at different radial distances, and thus the spatial reach, depend on the competition between these two opposing effects. Biophysical forward modelling revealed that, for uncorrelated synaptic LFP sources, the spatial reach (defined as the radius around the electrode containing the neuronal sources that provide 95% of the LFP amplitude) was about $200\mu m$. By contrast, for correlated neural LFP sources, which were induced by driving the neurons in the populations with correlated synaptic inputs, the situation was very different: here, distant sources dominated owing to a constructive interference effect between the single-neuron LFP sources, and the LFP signal increased without bounds with increasing population size. Thus, in this case the spatial reach of a recorded LFP is mainly set by the spatial extent of the pool of surrounding, correlated neural sources. The correlation level also determines the vertical LFP profile: correlated (and spatially asymmetrical) synaptic inputs generate a dipole-like LFP profile that spans the full vertical extent of the neural population, whereas homogeneous and/or uncorrelated inputs generate an LFP that is localized around the position of the synaptic inputs.

4.2 EXPERIMENTAL SETUP

The LFPs are recorded using a low impedance extracellular microelectrode, which measures the electrical potential difference (in volts) between the tissue and a reference electrode placed relatively near the recording electrode.
The operation principle of the multi-electrode-arrays used in the experiments analyzed in this thesis is an extended CMOS based EOSFET (Electrolyte Oxide Semiconductor Field Effect Transistor). The recording sites are arranged in rows and columns along the tip of the needle of the chip, in order to obtain spatial resolution. The number of recording sites is 256, organized in a rectangular shaped array (4×64). The recording electrodes were chosen to be $7.4\mu m$ in diameter size and octagonal in shape. The latter represented a tradeoff between the biological demand, as round shapes fulfill the best coverage ratio (i.e., the portion of the neuronal membrane attached to the recording electrode), and the technological limitations, since round structures cause problems during fabrication. The needle thickness was chosen to be $150\mu m$, as a compromise between maximum needle robustness and minor tissue damage during insertion. Accordingly to the dimensions of the recording array, the needle is chosen to be $300\mu m$ in width and $10mm$ long. The pitch (i.e. the distance between adjacent recording sites) was determined only by the required spatial resolution of the experiments. The selected x- and y-pitch was $33\mu m$ for the 4×64 rectangular arrays. For simultaneous recording from all the recording sites at least 256 interconnects were required, plus some voltage supply interconnects. To reduce the amount of contact pads needed, thus minimizing the huge contact area, a multiplexing approach was used.

As said, the 256 recording sites are organized in rectangular shaped arrays (4×64), while the underlying electrical circuit is arranged as a 16×16 matrix, each row being externally connected to one of 16 independent, custom-made transimpedance amplifiers (TIA), which record and amplify the overall current from the rows. By applying a proper sequence of biasing voltages on the columns, the 16 recording transistors of each row are then time-multiplexed, by sequentially switching on one transistor at a time, while leaving the other ones off. The multiplexed signals are then digitized by a NI PXIe-6358 (National Instruments) up to 1.25MS/s at 16bit resolution and saved to disk by a custom LabVIEW acquisition software.
Due to the in-vivo application of these devices, biostability and biocompatibility of the chip materials were required. A thin layer of TiO2 (30 nm-thick) was deposited over the silicon surface in a way that the needle chip did not impair the neural tissue and viceversa.
The chip was implanted in the somatosensory barrel cortex of the anesthetized rat, and vibrissa displacement controlled by a piezoelectric actuator.

CHAPTER 5

METHODS AND RESULTS

The recordings of the analyzed LFPs are 10 seconds long (9764 temporal frames), and twenty repetitions are available for each experiment. Recordings in which the whisker is stimulated two times are analyzed for five different rats; the inter-stimulus interval (ISI) is of two seconds. Every recording of this kind is subdivided in three intervals, in order to analyze the subsequent responses to the stimuli. The first interval covers the time within the response to the first stimulus and two seconds after that. The second covers the time within the response to the second stimulus and two seconds after that. Finally, the third interval goes from the end of the second interval to the end of the recording, and can be considered a *resting state* phase.
Likewise, recordings of *resting state*, in which no stimulus has been given to the anaesthetized rat, have been analyzed for four different rats.

5.1 AVALANCHES

Statistics of neuronal avalanches are computed in the recordings divided in three intervals and in the recordings of resting state. The standard method to detect avalanches requests thresholding of the time-series, to extract discrete events from continuous ones. So, for every electrode from the 4×55 array (9 columns of the array are not considered in the analysis as they are outside the barrel cortex), the mean and the standard deviation of the trace are computed over the whole time-series. Then, positive and negative excursions beyond a threshold are identified, and all points beyond the threshold are considered as events. The threshold chosen is ± 3 standard deviations (STD), following previous works ([29]), which showed that comparison of the signal distribution to the best fit Gaussian indicates that the two distributions start to deviate from one another at ~ 3 STD, therefore, thresholds smaller will lead to the detection of many events related to noise in addition to real events, whereas much larger thresholds

will miss many of the real events.

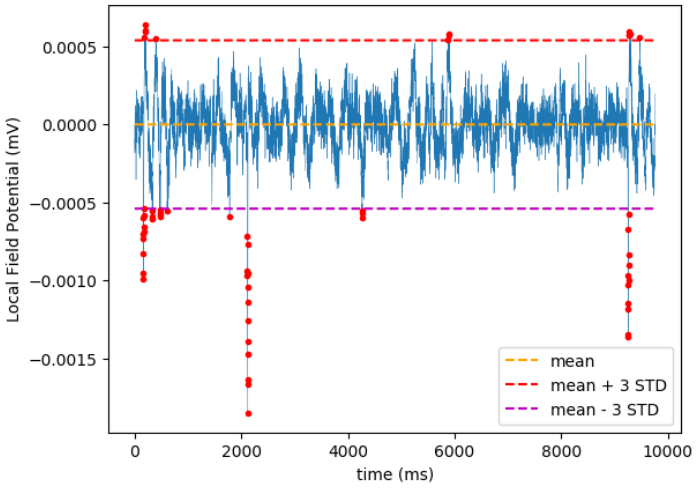

FIGURE 5.1: Example of the thresholding of the time series. The points marked with a red dot are considered events, so their value is set to 1. All the other points of the time series are instead set to 0.

The events are now called *peaks*. Then, the average inter-peak interval is computed (ΔT), and used to define avalanches: spatio-temporal clusters of consecutive LFP peaks with inter-peak interval not exceeding the temporal threshold ΔT. An avalanche duration is defined as the difference between the first and last LFP peak time within the avalanche, while the size of an avalanche is defined as the number of LFP peaks comprising the avalanche.

5.1.1 POWER-LAW FITTING

Following [19], we use a discrete distribution function to fit the distribution of avalanche sizes:

$$P(S) = S^{-\tau}(\sum_{x=x_0}^{x_M} x^{-\tau})^{-1}$$

where x_M is assumed to be the largest observed size and x_0 is set to 1. As avalanche duration is a non-integer variable, the fitting function for the duration distribution is

$$D(T) = (1-\alpha)(y_M^{(1-\alpha)} - y_0^{(1-\alpha)})T^{-\alpha}$$

with y_M the largest observed duration and y_0 set to 1. The fitting method maximizes the likelihood of the distributions $P(S)$ and $D(T)$ (in the next lines called generically $P_{param}(x)$) as functions of the parameters τ for the sizes distribution or α for the duration distribution. In a sample of n avalanches, assuming that the avalanches are independent, the likelihood of each model, given a parameter α or τ, is as follows:

$$L(param|x) = \prod_{i=1}^{n} P_{param}(x_i)$$

After finding the best-fit power law, the next step is to assess goodness of fit. The experimental data are compared against 1000 surrogate data sets drawn from the best-fit power-law distribution with the same number of samples as the experimental data set. The deviation between the surrogate data sets and a perfect power-law is quantified with the Kolmogorov Smirnov distance (KS).

$$KS = \sup_x |P_{fit}(x) - P_{data}(x)|$$

where P_{data} is the cumulative distribution from the data, and P_{fit} is the one computed from the fit. The quality q of the power-law fit is defined as the fraction of these surrogated KS statistics which are greater than the KS statistic for the experimental data. The criterion used for judging the data to be power-law distributed is $q > 0.1$, following the work done by the authors in Ref. [19].
Figure 5.2 shows an example of the results, as regard the size distribution of the avalanches for an experiment with an ISI of two seconds, in the three intervals (the histograms are presented with logarithmic scale on the x and on the y axes), while 5.3 shows the results for the duration distribution of the avalanches in the three intervals. Fig. 5.4 shows these same results, but referred to a resting state experiment. The exponents derived from the power-law fits, which respect the fit quality criterion $q > 0.1$, are presented in Table 5.1.
Moreover, in Fig. 5.5 the sizes of the avalanches are plotted (in logarithmic scale both on the x and on the y axis) versus the corresponding durations (every point represent an avalanche) for the experiment with an ISI of two seconds (A) and for the experiment of resting state (B). The different colors of the points in Fig. 5.5 (A) refer to the first, second and third interval. The predictions $S(T) = T^{\delta}$ where δ is given by $\delta = \frac{(\alpha-1)}{(\tau-1)}$ are also plotted. All these results refer to a single rat.
Figure 5.6 shows instead the exponents obtained analyzing data from different rats.

TABLE 5.1

	τ	α
I interval	1.53 ± 0.01	1.80 ± 0.02
II interval	1.61 ± 0.02	1.89 ± 0.02
III interval	1.63 ± 0.01	1.90 ± 0.01
resting state	1.62 ± 0.01	1.90 ± 0.01

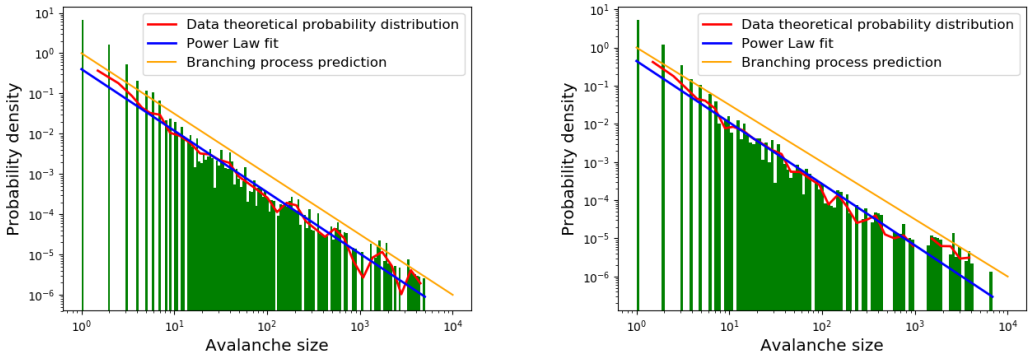

(A)

(B)

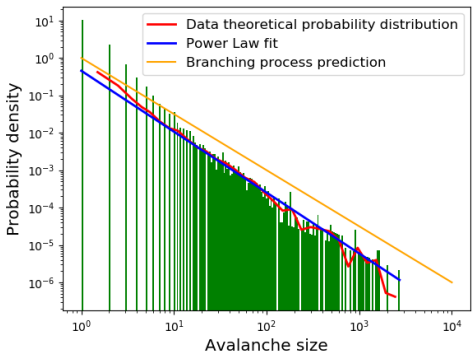

(C)

FIGURE 5.2: Avalanche sizes distributions in the interval after the first stimulus (A), after the second stimulus (B) and in the final part of the recording (C).

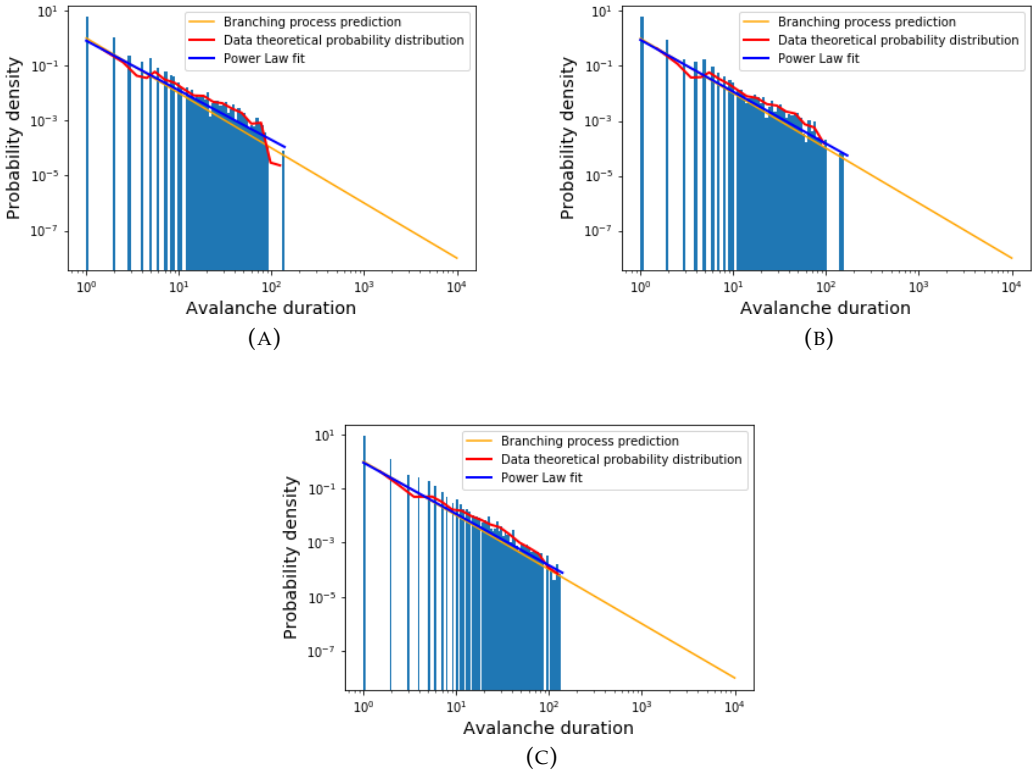

FIGURE 5.3: Avalanche durations distributions in the interval after the first stimulus (A), after the second stimulus (B) and in the final part of the recording (C).

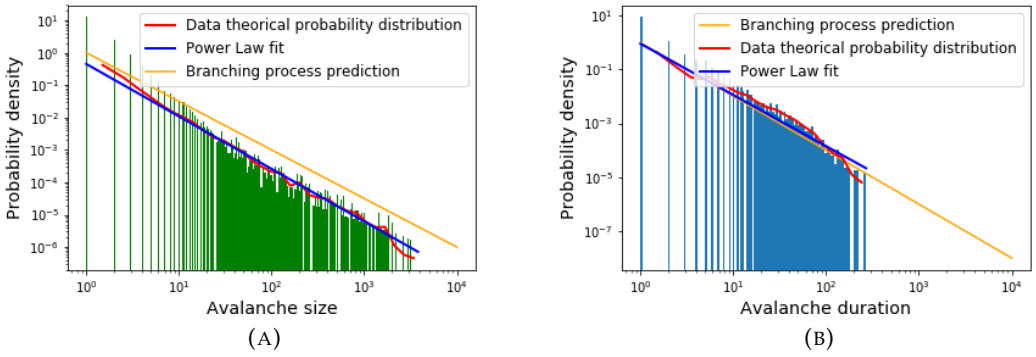

FIGURE 5.4: Sizes (A) and durations (B) distributions in a resting state experiment.

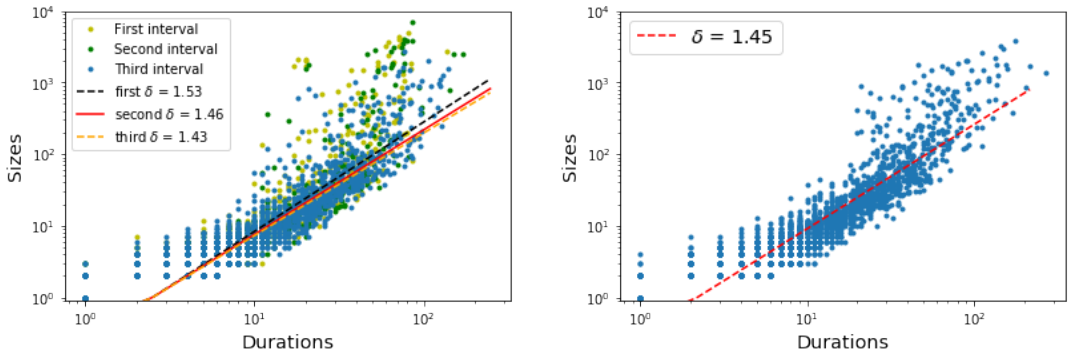

(A) (B)

FIGURE 5.5: Durations versus sizes of the avalanches in the experiment with a 2 seconds ISI, in the three intervals (A), and in the experiment of resting state (B) with the corresponding prediction $S(T) = T^{\delta}$ with δ given by $\frac{(\alpha-1)}{(\tau-1)}$.

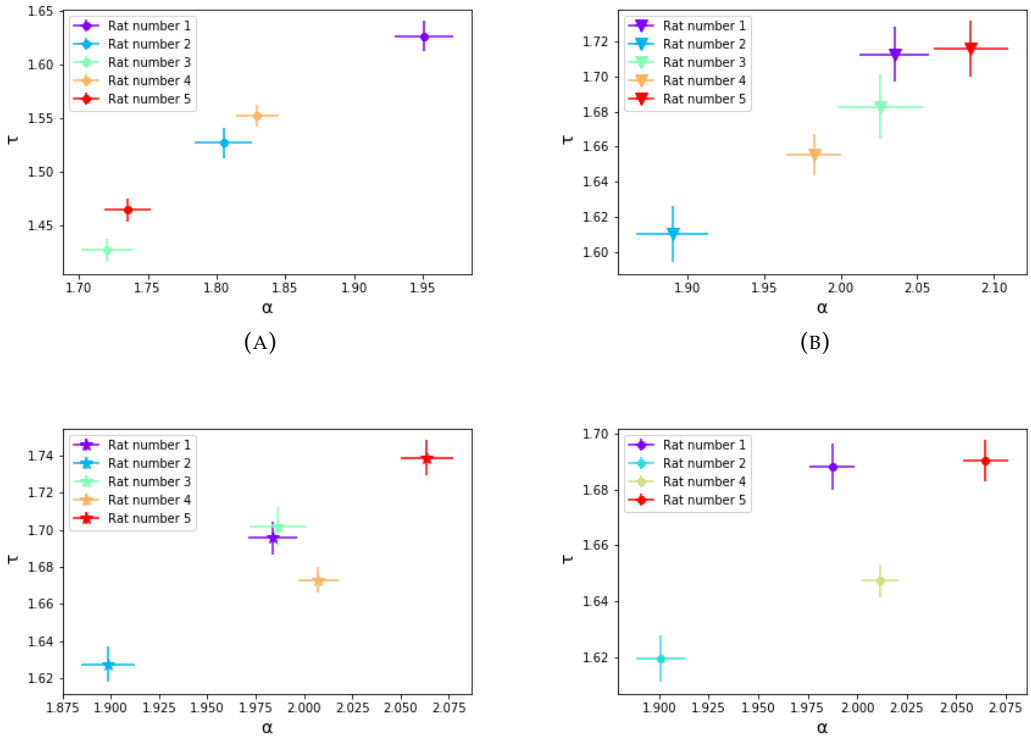

(A) (B)

(C) (D)

FIGURE 5.6: Exponents τ and α in the interval after the first stimulus (A), after the second stimulus (B) and in the final part of the recording (C) for five different rats; exponents in the resting state recording (D) for four rats. The corresponding values of $\delta = \frac{(\alpha-1)}{(\tau-1)}$ are 1.52, 1.53, 1.69, 1.50, 1.58 for Fig. (A), 1.45, 1.46, 1.50, 1.50, 1.51 for Fig. (B), 1.41, 1.43, 1.40, 1.50, 1.44 for Fig (C), 1.43, 1.45, 1.56, 1.54 for Fig (D).

5.2 SPATIAL CORRELATIONS

Exploiting the spatial information carried by the signal recorded in the different electrodes, spatial correlations are computed. The results here shown refer to a repetition of an experiment with an ISI of 2 seconds. No thresholding is applied to the signal, and the subdivision in three intervals is taken into account while computing the correlations. Thus, the spatial correlation matrix is obtained for the three intervals, computing the correlation coefficient between the signal v_i at the electrode i and the signal v_j at the electrode j, averaging over the whole time of the time-series within a interval:

$$C(i,j) = \frac{\langle v_i v_j \rangle_t - \langle v_i \rangle_t \langle v_j \rangle_t}{\sigma_i \sigma_j}$$

where σ indicates the standard deviation of the variable taken into account. The correlation matrix obtained are shown in Fig. 5.7 (A), (C) and (E).
Moreover, the correlation between two signals recorded at different locations is plotted as a function of the distance between the electrodes (which is expressed in unit of number of electrodes). The average over time in this case is computed reducing the time window (the first 500 frames are considered for each interval) in order to better capture the differences among the intervals after a stimulus and the resting state phase. The results obtained are shown in Fig. 5.7 (B), (D) and (F).

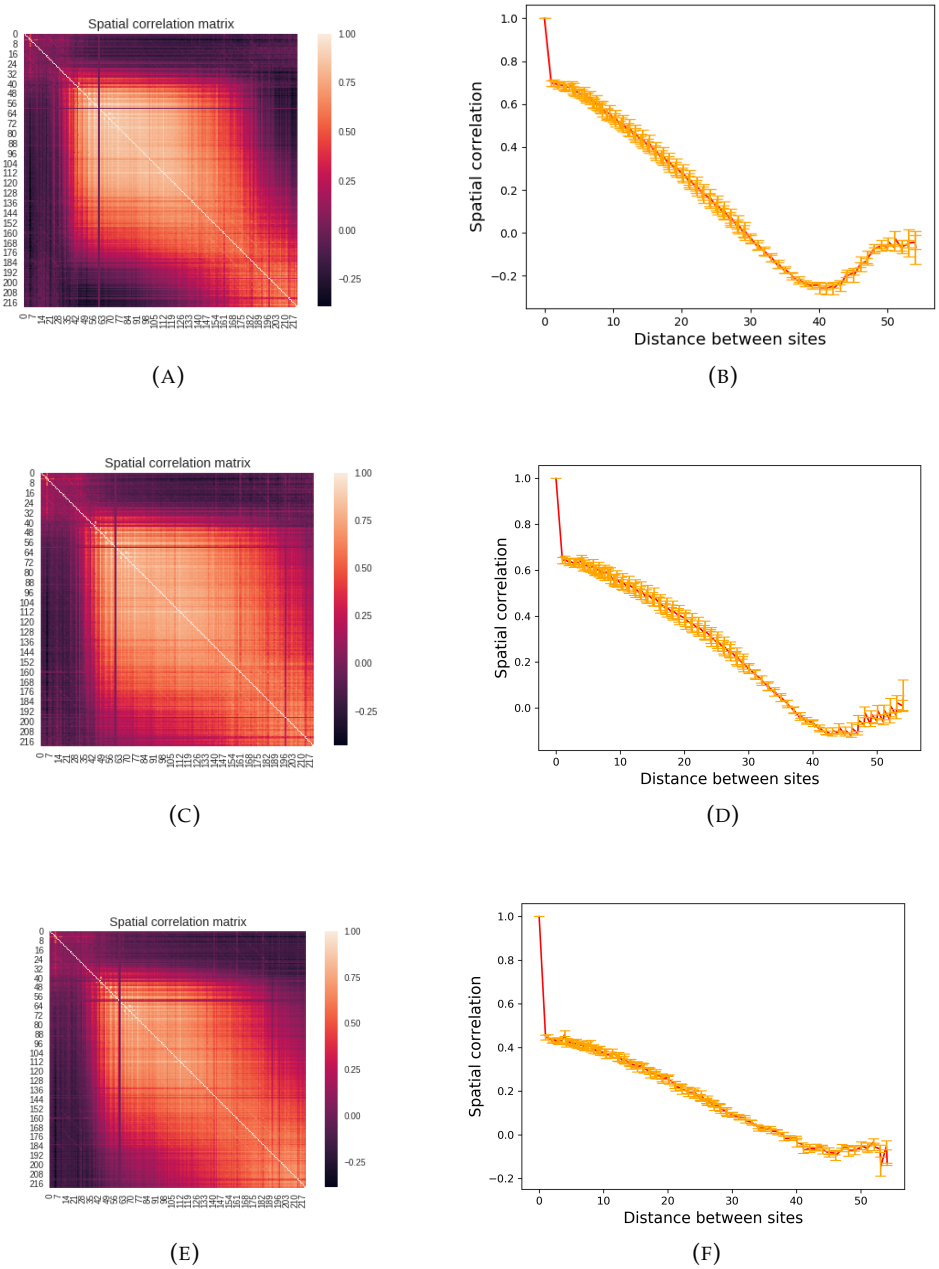

FIGURE 5.7: Spatial correlation matrix and corresponding trend of the correlation as a function of the distance between sites, in the interval after the first stimulus (A),(B), after the second stimulus (C),(D), and in the final part of the recording (E),(F).

5.2.1 PCA AND COARSE-GRAINING

A coarse-graining procedure based on Principal Component analysis is exploited, following the work done by the authors in ref [28]. They analyzed the data from an experiment that was able to monitor the single-cell activity of 1485 neurons in the hippocampus of a mouse moving in a virtual corridor for a long period of time. They discretized the activity so that cells are either "on", $v_i = 1$, or "off", $v_i = 0$. With enough resolution in time, this allows to look directly at the dynamical evolution of the population of neurons and to coarse-grain it.
The aim of the coarse-graining procedure is to reduce the number of degrees of freedom in the system, preserving as much as possible what is relevant in the data. PCA is probably the most dominant approach to dimensionality reduction. The idea is to think of the original variables v_i as living in a vector space, and then find the Euclidean projection onto a lower dimensional subspace that preserves as much of the total variance as possible.
The solution to this problem is to construct the covariance matrix

$$C_{ij} = \langle v_i v_j \rangle - \langle v_i \rangle \langle v_j \rangle$$

and then find the eigenvalues $\{\lambda_r\}$ and the eigenvectors $\{u_{jr}\}$

$$\sum_{j=1}^{N} C_{ij} u_{jr} = \lambda_r u_{ir}$$

with the eigenvalues ordered $\lambda_1 > \lambda_2 > \lambda_3$ etc. As usual we normalize the eigenvectors to unit length, and they are orthogonal, so that

$$\sum_{r=1}^{N} u_{ir} u_{jr} = \delta_{ij}$$

We can define operators $\hat{P}(K)$ that project onto the subspace spanned by the K eigenvectors associated with the K largest eigenvalues

$$\hat{P}_{ij}(K) = \sum_{r=1}^{K} u_{ir} u_{jr}$$

Finally, coarse-grained variables are defined by these projections:

$$v_i \to \tilde{v}_i = \sum_{j=1}^{N} \hat{P}_{ij}(K) v_j$$

The usual hope in using PCA is that the eigenvalue spectrum will point to a clear reduction of dimensionality. For this to happen, we need to see that the first D modes capture a large fraction of the total variance, that is $F(D)$ approaches unity for some small $D \ll N$, where

$$F(D) = \frac{\sum_{i=1}^{D} \lambda_i}{\sum_{j=1}^{N} \lambda_j}$$

and there is a gap in the spectrum between λ_D and λ_{D+1}.
Remarkably, that is indeed what emerges from our data. The results here shown refer to a repetition of an experiment with an ISI of 2 seconds. The covariance of the matrix X, which in our case is $N \times D$, with N number of temporal frames and D number of pixels in the array (each row represents a configuration of the array) is computed. A spectral gap emerges in the eigenvalues spectrum of the covariance matrix (Fig. 5.8 (A)), and, indeed, when computing the percentage of variance explained by each component (with the name "components" we refer to the eigenvectors of the covariance matrix) it results that the first two components explain the 60 % of the total variance (Fig. 5.8 (B)). A brief review of PCA and a more detailed account between its relation with the coarse-graining procedure is given in Appendix A.

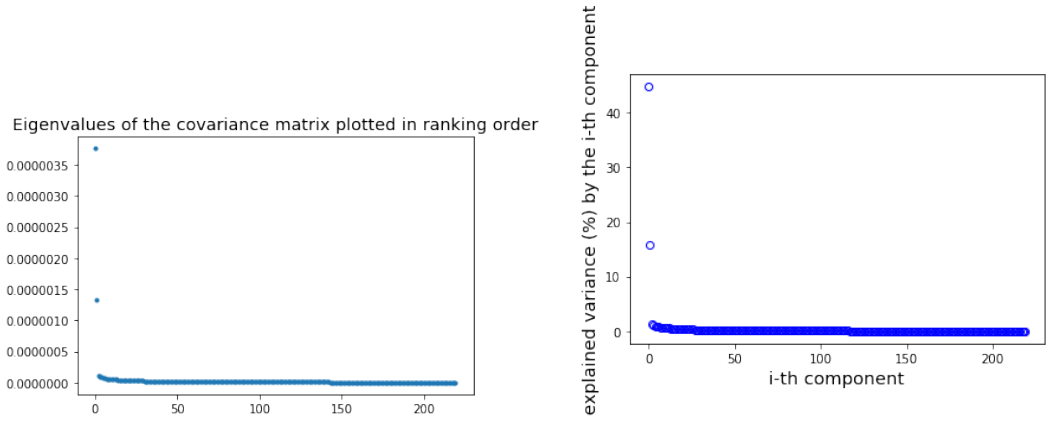

(A) (B)

FIGURE 5.8

To be more precise, the aim of the coarse-graining procedure is not merely to reduce dimensionality of the system, but to analyze what happens to the distribution of the coarse-grained variables as we move the boundary between the details that we average over and the more macroscopic features that we keep. Indeed, each step of coarse-graining is followed by an expansion of the system that restores the original number of variables, so that dimensionality reduction itself is never the goal. If the correlations in the system are sufficiently weak, then the central limit theorem guarantees that the distribution of coarse grained variables, as far as one reduces the cutoff K in the operator $\hat{P}(K)$ and averages over more and more details, will approach a fixed, Gaussian form. The strategy to achieve this goal is here described: at each moment in time, the activity recorded at each location i (in our case, in each recording electrode) in the population that we study is described by a variable v_i. We want to coarse-grain these variables and follow the flow of their probability distribution. The hope is to see that this distribution is approaching some non trivial fixed form as we average over more and more of the microscopic details. We can put the principal components in order by their contribution to the variance, and then averaging over the components that make small contributions to the variance is analogous to averaging over small

variance, short wavelength fluctuations. More precisely, we coarse-grain by placing a cutoff, keeping only those $\hat{K}$ principal components that make the largest contributions to the variance. Then we'll study what happens to the distribution of the remaining variables as we change the cutoff. Concretely, we start with the covariance matrix, C_{ij}, find eigenvalues and eigenvectors and then define coarse-grained variables as projections onto the subspace associated with the $\hat{K}$ largest eigenvalues.

$$\phi_i(\hat{K}) = z_i(\hat{K}) \sum_j \hat{P}_{ij}(\hat{K})[v_i^{(1)} - \left\langle v_i^{(1)} \right\rangle]$$

with $P_{ij}(\hat{K})$ the projection operator defined above. In order to track the distributions of these variables as we change our cutoff $\hat{K}$, it is easiest to subtract the mean, as done here, and choose $z_i(\hat{K})$ so that $\left\langle \phi^2_{\hat{K}}(i) \right\rangle = 1$.

$$z_i(\hat{K}) = \sqrt{\frac{1}{\sum_{jm} P_{ij} P_{im} [\langle v_i v_m \rangle - \langle v_i \rangle \langle v_m \rangle]}}$$

In this setting it is interesting to look at the joint distribution:

$$P_{\hat{K}}(\phi) = \frac{1}{N} \sum_i \mathbb{P}[\phi_i(\hat{K}) = \phi]$$

as we change the cutoff $\hat{K}$. In fact, as said in the previous lines, the coarse-graining procedure typically drives the joint probability distribution of a set of variables towards a fixed point, which for zero-mean and independent variables is exactly the Central Limit Theorem one.
This procedure is applied to our data (Fig. 5.9), and the results here presented refer to the same dataset studied in Fig. 5.8 (a repetition of an experiment with an ISI of 2 seconds between the stimuli). This procedure is applied both to the discretized time-series (applying a threshold as described in section 5.1), so that the variable v_i takes only the values 0 and 1, and to the signal without discretization, so that v_i is a continuous variable. Remarkably, in both cases the joint distribution of the coarse-grained variables seems to approach a non trivial fixed distribution, which deviates from a Gaussian one. That should remark the fact that the correlations in the system are stronlgy present and that the fixed point in this case is not given by the central limit theorem.

5.3 TEMPORAL CORRELATIONS

Temporal correlations are also studied. In particular, correlations between signals recorded at different times are computed averaging in space (over the values that the signal assumes over all the electrodes).

$$C(t, t + \Delta t) = \frac{\langle v_i(t) v_i(t + \Delta t) \rangle_i - \langle v_i(t) \rangle_i \langle v_i(t + \Delta t) \rangle_i}{\sigma(t) \sigma(t + \Delta t)}$$

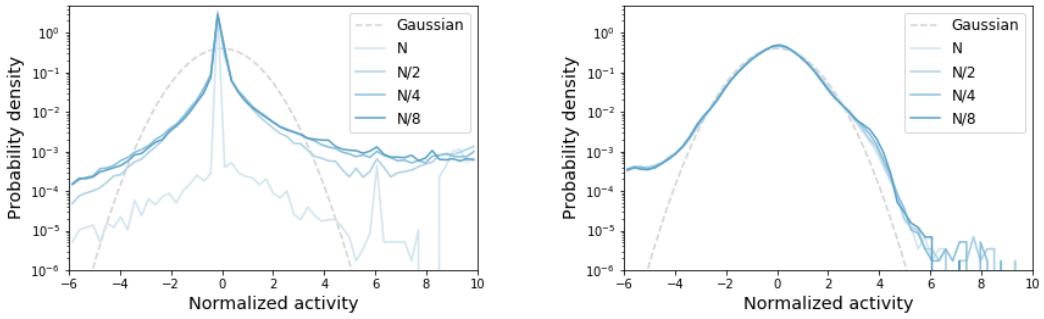

(A) (B)

FIGURE 5.9: Joint distribution of the variables $\phi_i(\hat{K})$, with a binary discretization of the variables v_i (A) and without discretization (B), reducing the cutoff $\hat{K}$ from N = 220 (number of the sites in the array 4 × 55), to $\frac{N}{8}$.

The values of the temporal correlations are shown as a function of the time interval between signals Δt in Fig. 5.10, considering at most a Δt of 1000 ms.
Moreover, the autocorrelation function of the signal for each electrode is computed:

$$C_i(t, t+\Delta t) = \frac{\langle v_i(t)v_i(t+\Delta t)\rangle_t - \langle v_i(t)\rangle_t \langle v_i(t+\Delta t)\rangle_t}{\sigma_i(t)\sigma_i(t+\Delta t)}$$

The results presented in Figure 5.11 show the mean of the autocorrelation function over all the electrodes, considering at most a Δt of 1000 ms. Noteworthy differences are observed among the three intervals. To better capture these differences, the power spectrum of these time-series is computed. The Wiener-Khinchin theorem indeed states that the power spectral density (or power spectrum, $S_v(f)$) of a signal (v) coincides with the Fourier transform of the autocorrelation function of the signal itself, which, in case of a wide-sense stationary process, depends only on the time interval difference Δt:

$$C_v(\Delta t) = \int_{-\infty}^{+\infty} S_v(f) e^{-i2\pi f \Delta t} df.$$

After computing the power spectrum of the time-series in the three intervals, the dominant frequencies are selected (the ones with the highest power spectral density) for each electrode. It results that for the majority of the electrodes in the first interval the dominant frequency is 7Hz. In the second and in the third interval instead the majority of the electrodes shows a dominant frequency of 3 Hz.

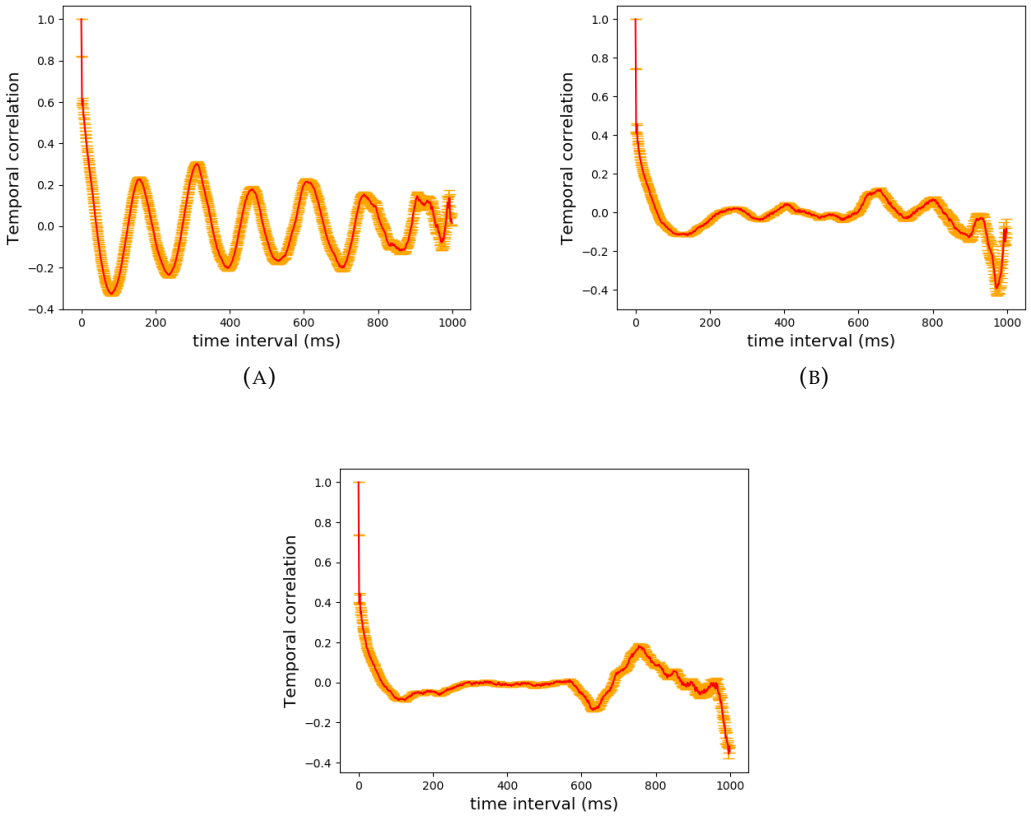

FIGURE 5.10: Temporal correlation as a function of the time difference Δt, in the interval after the first stimulus (A), after the second stimulus (B) and in the final part of the recording (C).

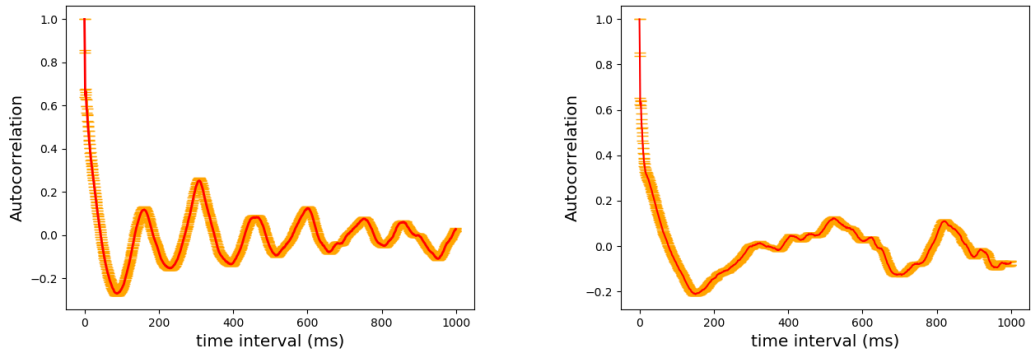

(A)

(B)

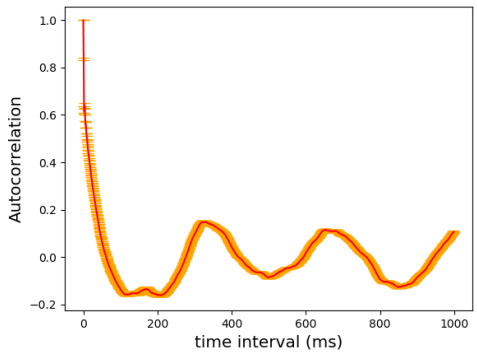

(C)

FIGURE 5.11: Autocorrelation function in the interval after the first stimulus (A), after the second stimulus (B) and in the final part of the recording (C).

5.4 Discussion of the Results on Correlations

As concerns the spatial correlations, it is noteworthy that strong correlations are present in the dataset taken into account, fact that emerges both from Figure 5.7 and from the coarse-graining procedure done in section 5.2.1. Moreover, from the Principal Component Analysis study it emerges that the dynamics is low dimensional, and that the dimensionality of the system could be reduced to the first two components and still describe the 60% of the variance of the data. From figure 5.7 a different trend in the three intervals emerges as regards the spatial correlation as a function of the distance: the intervals after a stimulus present an initial correlation, which decreases with distance, but that at a certain distance (about 40 electrodes) starts to increase again. This final aspect is not present in the resting state interval, where instead the spatial correlation decreases with distance until it reaches a plateu. This may result from the known existence of the dipole-currents that arise after a stimulus, due to synaptic currents in the deep cortical layers and the return capacitive currents at the level of dendritic branches in upper layers of the barrel column.
As regards temporal correlations and the autocorrelations functions it is observed that the interval after the second stimulus seems to have a behaviour more similar to the resting state than to the interval after the first stimulus, which instead displays a sinusoidal behaviour both in the temporal correlations averaging in the space and in the autocorrelation. This fact is probably strictly linked to the ISI of two seconds, and it is discussed also in chapter 6 as regards neuronal avalanches. This aspect is also investigated studying the power spectrum of the time series in the three intervals, which indeed seems to highlight that the dominant frequency in the first interval is higher (7 Hz) than the one in the next two intervals (3 Hz).

CHAPTER 6

CONCLUSIONS AND FUTURE PERSPECTIVES

The results presented in section 5.1 show a power-law behaviour of the sizes and lifetimes distributions of the avalanches, both in the resting state interval and in the post stimuli intervals. Moreover, the scaling of the size of the avalanches with respect to the corresponding duration $S(T) = T^{\delta}$ is compatible with the prediction $\delta = \frac{(\alpha-1)}{(\tau-1)}$ (Fig. 5.5). Thus, we find consistent markers of criticality in the scaling of avalanche statistics. However, our results are incompatible with a phase transition between a quiescent and an active state, typical of the MF-DP class (the universality class of the branching process). This fact emerges from Table 5.1 and from Figure 5.6: the exponents of the power laws deviates from the predicted $\tau = \frac{3}{2}$ and $\alpha = 2$, in particular as regard the sizes distributions, which, in the majority of the cases, are characterized by exponents higher than $\frac{3}{2}$. It is noteworthy that these results are close to recently obtained ones from the LFPs of the ex-vivo visual cortex of turtles [19] and to the experimental exponents derived in [31] from neuronal data of rat cortex collected at the individual neuron level. The deviation from the MF-DP class is more evident when observing the results in the sizes versus durations plane (Fig. 5.5): the predicted δ for the branching process is 2, while from our data the value of δ is close to 1.5. This result is consistent with the recent studies in [19], in [31], and with studies on the primary visual cortex of urethane-anaesthetized rats [24]. In Ref. [24] they also highlight a disagreement with the MF-DP class, that is evident from a value of δ significantly lower than 2. The authors indeed support a scenario in which the transition governing brain dynamics is not between absorbing and active phases, but rather between a phase in which neurons fire synchronously and a phase characterized by largely incoherent firing of neurons.
Moreover, deviations from power law are not observed in the post stimuli intervals,

while it has been proposed that the sensory input may elicits network activity that is not critical. No remarkable differences are neither observed in Fig. 5.5 (A), where the sizes of the avalanches are plotted versus the corresponding durations for the three intervals, together with the predictions $S(T) = T^{\delta}$ with $\delta = \frac{(\alpha-1)}{(\tau-1)}$: in each case the prediction is compatible with the data. However, consistently with the hypothesis that the sensory input could increase the overall activity of the neurons, the main difference observed in post stimuli intervals with respect to the resting state ones is that the first present lower exponents both for the sizes and for the lifetimes distribution. This indicates that after a stimulus the population of neurons shows longer avalanches and with more events, than in resting state. To be more precise, this aspect emerges prominently when comparing the exponents of the interval after the first stimulus with the next two intervals: the response to the second stimulus seems attenuated by the first one, and the interval after the second stimulus seems more similar to a resting state phase, as it has been noted in Section 5.4 as regards temporal correlations. This fact is probably strictly determined by the ISI of two seconds: it has been noted that a shorter ISI could increase the response to the second stimulus, while a longer ISI may not affect the second response. An ISI of two seconds instead has probably the effect to strongly reduce the rensponse to the second stimulus. Further work could be done in this perspective, studying the effects on the avalanches and on the correlations when in presence of two stimuli, considering a varying ISI.
As a preliminary analysis for a future study, avalanches are also computed considering separately the signals recorded in the different layers of the barrel cortex, and the sizes and lifetimes distributions are studied. The power-law exponents obtained are shown in Table 6.1 as regards the sizes, and in Table 6.2 as regards the lifetimes, and in this case the time-series are only divided in two intervals: one including the responses to the first stimulus and to the second, and one covering the remaining recording of resting state. The exponents here presented are obtained averaging over the results of five rats.

TABLE 6.1: τ exponents

	Post stimuli	Resting state
Layer I	1.67 ± 0.01	1.73 ± 0.01
Layer II	1.31 ± 0.005	1.61 ± 0.01
Layer III	1.0025 ± 0.0001	1.55 ± 0.01
Layer IV	1.0000 ± 0.0001	1.53 ± 0.01
Layer Va	1.327 ± 0.005	1.58 ± 0.01
Layer Vb	1.49 ± 0.01	1.57 ± 0.01
Layer VI	1.49 ± 0.01	1.59 ± 0.01

This further analysis shows additional interesting information: as remarked in Chapter 3, layer IV neurons are intrinsic elements of all the microcircuits that encode tactile input from the whiskers. Consistently with that, the exponents of the sizes (and lifetimes) distributions referring to the electrodes in layer IV are smaller than the ones in the layers above and below, and so the distributions result broader. Moreover, in

TABLE 6.2: α exponents

	Post stimuli	Resting state
Layer I	1.77 ± 0.01	1.80 ± 0.01
Layer II	1.58 ± 0.01	1.74 ± 0.01
Layer III	1.49 ± 0.01	1.75 ± 0.01
Layer IV	1.48 ± 0.01	1.75 ± 0.01
Layer Va	1.57 ± 0.01	1.72 ± 0.01
Layer Vb	1.65 ± 0.01	1.68 ± 0.01
Layer VI	1.64 ± 0.01	1.67 ± 0.01

this analysis a more marked difference between post stimulus interval and resting state seems to emerge.
All in all, we have presented an analysis of neuronal avalances in the rat barrel cortex, both at resting states and after perturbation, and of the spatial and temporal correlations of the neural activities. We find consistent signatures of criticality in the power-law scaling of the neuronal avalanches and in the strong correlations in the system that emerged from the study (see Fig. 5.7) and from the coarse-graining procedure. Scaling consistent with criticality is found both at resting state and after the whisker stimulation. When visualizing the data in the sizes versus durations plane, a deviation from the predictions of the MF-DP universality class becomes more clear, fact that supports the recently moved hypothesis [24] that the critical point at which the brain dynamics would be poised is not between an active and a silent activity phase. These results, together with the complex behaviour of the spatial correlations (Fig. 5.7) and with the different roles that the different layers of the barrel cortex might play on criticality (as seen in Table 6.1 and 6.2), suggest future theoretical studies to better characterize the dynamics of the barrel cortex neural circuit. In particular, we aim at building a network model, which includes diverse layers, in order to reproduce the observed behaviour and to understand better the principles that could govern criticality in the rat barrel cortex.

APPENDIX A

PRINCIPAL COMPONENT ANALYSIS

Let us denote by X_{ij} the $P \times N$ matrix of P points each with N features, so each row represent a single configuration x_i that lives in a $N-$dimensional space. Singular value decomposition tells us that every $P \times N$ matrix can be written as:

$$X = U\Sigma V^T, \quad UU^T = \mathbb{1} = VV^T, \quad \Sigma = diag(\sigma_1, ..., \sigma_r)$$

where $U \in \mathbb{M}(P \times P)$, $V \in \mathbb{M}(N \times N)$, $\Sigma \in \mathbb{M}(P \times N)$ and $r = \min(P, N)$ [30]. The values $(\sigma_1, ..., \sigma_r)$ are called singular values of the matrix X, whereas the columns of U and V are respectively called the left-singular vectors and the right -singular vectors of X. In fact, we shall notice that

$$\begin{cases} X^T X = V\Sigma^T\Sigma V^T, & \Sigma^T\Sigma \in \mathbb{M}(N \times N) \\ XX^T = U\Sigma\Sigma^T U^T, & \Sigma\Sigma^T \in \mathbb{M}(P \times P) \end{cases}$$

which means that the right-singular vectors of X are eigenvectors of $X^T X$, and the left-singular vectors are eigenvectors for XX^T. This further implies that the non-zero singular values of X are the square roots of the non-zero eigenvalues of both XX^T and $X^T X$.
With this in mind, a possible approach to dimensionality reduction is to find the best low-rank decomposition of X, where we should note that the rank is equal to the number of non-zero singular values. We want:

$$\min ||X - X_k||_F^2 = \min[\sum_{ij}(X - X_k)_{ij}^2]$$

where X_k is a rank k matrix. Let us look for a unitary rank decomposition

$$X_1 = \lambda \mathbf{a}\mathbf{b}^T, \quad \mathbf{a}^T\mathbf{a} = 1 = \mathbf{b}\mathbf{b}^T \tag{A.1}$$

with $\mathbf{a} \in \mathbb{R}^P$ and $\mathbf{b} \in \mathbb{R}^N$ so that X_k is a $P \times N$ matrix. Hence

$$\partial_{b_\mu}[\sum_{ij}(X_{ij} - \lambda a_i b_j)^2] = 0 = a_i \sum_i (X_{i\mu} - \lambda a_i b_\mu)$$

and, upon deriving with respect to the components of a as well, we end up with

$$\begin{cases} \mathbf{a}^T X = \lambda \mathbf{b}^T \\ X\mathbf{b} = \lambda \mathbf{a} \end{cases}$$

from which follows:

$$\begin{cases} XX^T\mathbf{a} = \lambda^2 \mathbf{a} \\ X^T X\mathbf{b} = \lambda^2 \mathbf{b} \end{cases}$$

This results means that equation A.1 is the best rank 1 decomposition of X if $\mathbf{a}$ is an eigenvector of XX^T and $\mathbf{b}$ is an eigenvector of X^TX, both with the same eigenvalue λ^2. Hence we can write:

$$X_1 = \sigma_i \mathbf{u}_i \mathbf{v}_i^T$$

for some $i = 1, ...,$ rank(X). The only thing we need to do is to choose the appropriate index i among them. Since $X = \sum_j \sigma_j \mathbf{u}_j \mathbf{v}_j^T$ and the Frobenius norm is defined as $||X||_F^2 = \sum_i \sigma_i^2$, it is clear that the quantity $||X - X_1||_F^2$ is minimized if we choose the index i to be the one of the highest singular value. In fact,

$$||X - X_1||_F^2 = ||X - \sigma_i \mathbf{u}_i \mathbf{v}_i^T||^2 = \sum_{j=1, j\neq i}^{rank(X)} \sigma_j^2$$

so the best choice we can make is to remove from this sum the highest singular value. This is known as the Young-Eckhart theorem and it is true for any value k: if $i = 1, ..., k$ are the indexes of the highest singular values and we define:

$$X_k = \sum_{i=1}^{k} \sigma_i \mathbf{u}_i \mathbf{v}_i^T$$

then $||X - X_k||_F < ||X - B||_F$ for every matrix $B \in \mathbb{M}(P \times N)$ of rank k. Hence, the low-rank decomposition is intimately related to the k highest singular values.
Insofar, we said nothing about dimensionality reduction, albeit it is clear that finding a rank $k < N$ decomposition amounts to restrict the data into a $k-$dimensional subspace of the original $N-$dimensional space. Thus, in light of the Young-Ekchart theorem, instead of finding a rank k decomposition we could directly project the variables into the subspace spanned by the k highest right-singular vector of X. This is what PCA does when it is used to reduce the dimensionality of the data.
Suppose that $P > N$, that is we have more points that dimensions. Then the rank of X

is at most N. Reducing the dimensionality amounts to find a matrix $X_{P,k} \in \mathbb{M}(P \times k)$ which represents P points in k dimensions. To do so we introduce the $N \times k$ matrix

$$W = (\mathbf{v}_1, ..., \mathbf{v}_k)$$

where $\mathbf{v}_i$, being right-singular vectors, are the eigenvectors of $X^T X$. For the sake of argument, suppose that the data are centered: then $X^T X$ is exactly the covariance matrix, and W is the matrix of the k of the highest eigenvalues of the covariance matrix. Thus, the low dimensional representation is:

$$X_{P,k} = XW \in \mathbb{M}(P \times k).$$

W is called the matrix of the principal directions, and $X_{P,k}$ gives the first k principal components. For instance, an usual choice is $k = 2$ so that we can plot the first two principal components versus each other. Noice that by means of the Young-Eckhart theorem this would be the best two-dimensional representation of the data, but nothing tells us a priori that the data really live in two dimensions. We need to look at the spectrum of $X^T X$ to understand whether is makes sense or not.
Finally, let us remark that what we do in our coarse-graining, where we vary a cutoff on the number of eigenvectors we project onto, is essentially equivalent to determine the best low-rank decomposition rather than dimensionality reduction. In fact, in the notation used for the singular value decomposition, the projector we used in Chapter 5 is given by:

$$(P_k)_{\mu\nu} = \sum_{i=1}^{k} v_{\mu i} v_{\nu i}$$

But then we recover the result of the Young-Eckhart theorem by means of

$$X_k = XP_k = \sum_{j=1}^{r} \sigma_j \mathbf{u_j} \mathbf{v}_j^T \sum_{i=1}^{k} \mathbf{v}_i \mathbf{v}_i^T = \sum_{i=1}^{k} \sigma_i \mathbf{u}_i \mathbf{v}_i^T$$

Hence, if we define the $P \times N$ matrix Φ as the matrix of the coarse-grained variables we have:

$$\Phi_{\mu\nu} = \sum_{\sigma=1}^{N} X_{\mu\sigma} (P_k)_{\sigma\nu}$$

which is exactly X_k.

BIBLIOGRAPHY

[1] M. A. Muñoz, "Colloquium: Criticality and dynamical scaling in living systems", In: *Reviews of modern physics*, vol 90 (2018)

[2] D. R. Chialvo, "Emergent complex neural dynamics", In: *Nature Physics*, vol 6 (2018)

[3] J. M. Beggs and D. Plentz, "Neuronal Avalanches in Neocortical Circuits", In: *The journal of neuroscience*, 23(35):11167-11177 (2003)

[4] J. Touboul and A. Destexhe, "Power-law statistics and universal scaling in the absence of criticality", In: *Physical Review E* 95 (2017)

[5] J. Hidalgo, J. Grilli, S. Suweis, M. A. Muñoz, J. R. Banavar, and A. Maritan "Information-based fitness and the emergence of criticality in living systems", In: *Proceedings of the National Academy of Sciences* 111 (28), 10095-10100 (2014)

[6] O. Kinouchi and M. Copelli, "Optimal dynamical range of excitable networks at criticality", In: *Nature Physics* 2, 348-351 (2006)

[7] A. Mazzoni, F. D. Broccard, E. Garcia-Perez, P. Bonifazi, M. E. Ruaro, and V. Torre, "On the Dynamics of the Spontaneous Activity in Neuronal Networks", In: *PLoS One* 2 (2007)

[8] V. Pasquale, P. Massobrio, L. Bologna, M. Chiappalone, and S. Martinoia, "Self-organization and neuronal avalanches in networks of dissociated cortical neurons", In: *Neuroscience* 153 (2008)

[9] E. D. Gireesh and D. Plenz, "Neuronal avalanches organize as nested theta- and beta/gamma-oscillations during development of cortical layer 2/3", In: *Proceedings of the National Academy of Sciences U.S.A.* 105 (2008)

[10] T. Petermann, T. A. Thiagarajan, M. Lebedev, M. Nicolelis, D. R. Chialvo, and D. Plenz, "Spontaneous cortical activity in awake monkeys composed of neuronal avalanches", In: *Proceedings of the National Academy of Sciences U.S.A.* 106 (2009)

[11] G. Hahn, T. Petermann, M. N. Havenith, S. Yu, W. Singer, D. Plenz, and D. Nikolic, "Neuronal Avalanches in Spontaneous Activity In Vivo", In: *Journal of Neurophysiology* 104 (2010)

[12] T. L. Ribeiro, M. Copelli, F. Caixeta, H. Belchior, D. R. Chialvo, M. A. L. Nicolelis, and S. Ribeiro, "Spike Avalanches Exhibit Universal Dynamics across the Sleep-Wake Cycle", In: *PLoS One 5* (2010)

[13] S. Yu, H. Yang, H. Nakahara, G. S. Santos, D. Nikolic, and D. Plenz, "Higher-Order Interactions Characterized in Cortical Activity", In: *The Journal of Neuroscience* 31 (2011)

[14] L. Onsager, "Crystal Statistics. I. A Two-Dimensional Model with an Order Disorder Transition", In: *Phys. Rev*. 65:3-4 (1944).

[15] K. Huang. *Statistical Mechanics*. Wiley, 1987

[16] W. L. Shew and D. Plentz, "The Functional Benefits of Criticality in the Cortex", In: *The Neuroscientist* vol 19(1):88-100 (2013)

[17] J. M. Beggs and N. Timme, "Being critical of criticality in the brain", In: *Frontiers in Physiology*, vol 3.163 (2012).

[18] A. Levina, J. M. Herrmann and T. Geisel, "Dynamical synapses causing self-organized criticality in neural networks", In: *Nature Physics* vol 3:857-860 (2007)

[19] W. L. Shew, W. P. Clawson, J. Pobst, Y. Karimipanah, N. C. Wright, and R. Wessel, "Adaptation to sensory input tunes visual cortex to criticality", In: *Nature Physics* vol 11 (2015)

[20] J. P. Sethna, K. A. Dahmen and C. R. Myers. "Crackling noise", In: *Nature* vol 410, p. 242-250 (2001).

[21] P. Villegas, S. di Santo, R. Burioni and M. A. Muñoz, "Timeseries thresholding and the definition of avalanche size", In: *Phys. Rev. E* vol 100 (2019)

[22] H. Linden et al. "Modeling the spatial reach of the LFP", In: *Neuron* vol 72, p. 859-872 (2011).

[23] G. T. Einevoll, C. Kayser, N. K. Logothetis and S. Panzeri, "Modelling and analysis of local field potentials for studying the function of cortical circuits", In: *Nature reviews* vol 14, p. 785 (2013)

[24] A. J. Fontenele, N. A. P. de Vasconcelos, T. Feliciano, L. A A. Aguiar, C. Soares-Cunha, B. Coimbra, L. Dalla Porta, S. Ribeiro, A. J. Rodrigues, N. Sousa, P. V. Carelli, and M. Copelli, "Criticality between Cortical States", In: *Physical review letters* vol. 122, 208101 (2019)

[25] S. Zapperi, K. B. Lauritsen, and H. E. Stanley, "Self-Organized Branching Processes: Mean-Field Theory for Avalanches", In: *Phys. Rev. Lett.* vol. 75 (1995)

[26] D. Feldmeyer, M. Brecht, F. Helmchen, C. C. H. Petersen, J. F. A. Poulet, J. F. Staiger, H. J. Luhmann, C. Schwarz, "Barrel cortex function", In: *Progress in Neurobiology*, vol 103:3-27 (2013)

[27] C. C. H. Petersen, "The Functional Organization of the Barrel Cortex", In: *Neuron*, vol 56 (2007)

[28] L. Meshulam et al. "Coarse-graining and hints of scaling in a population of 1000+ neurons", In: arXiv preprints (2018). eprint: 1812.11904 (physics.bio-ph).

[29] O. Shriki et al. "Neuronal Avalanches in the Resting MEG of the Human Brain", In: *The Journal of Neuroscience*, 33(16):7079-7090 (2013)

[30] Y. S. Abu-Mustafa, M. Magdon-Ismail and L. Hsuan-Tien, "Learning from Data", AMLbook (2012)

[31] N. Friedman et al. "Universal critical dynamics in high resolution neuronal avalanche data", In: *Physical Review Letters* vol. 108 (2012)

[32] K. B. Lauritsen, S. Zapperi, and H. E. Stanley, "Self-organized branching processes: Avalanche models with dissipation", In: *Physical Review E* vol 54 (1996)

[33] B. G. Cragg, H. N. Temperley, "The organisation of neurones: a co-operative analogy", In: *Electroencephalogr. Clin. Neurophysiol.* vol 6:85-92 (1954)

[34] B. G. Cragg, H. N. Temperley, "Memory: the analogy with ferromagnetic hysteresis", In: *Brain* vol 78:304-16 (1955)

[35] A. Herz, J. Hopfield, "Earthquake cycles and neural reverberations: collective oscillations in systems with pulse-coupled threshold elements", In. *Physical Review Letters* vol 75:1222-5 (1995)

[36] S. di Santo et al., "Landau-Ginzburg theory of cortex dynamics: Scale-free avalanches emerge at the edge of synchronization.", In: *Proceedings of the National Academy of Sciences* vol 115.7 (2018)

[37] J. D. Amit, "Modeling brain function: The world of attractor neural networks", Cambridge University Press, NY (1989)

[38] P. Bak, "How Nature Works: the science of self-organized criticality", Copernicus, New York, 1996

[39] C. Meisel, E. Olbrich, O. Shriki and P. Achermann, "Fading Signatures of Critical Brain Dynamics during Sustained Wakefulness in Humans" In: *Journal of Neuroscience* vol 33 (2013)